



UNIVERSIDADE ESTADUAL DE CAMPINAS  
SISTEMA DE BIBLIOTECAS DA UNICAMP  
REPOSITÓRIO DA PRODUÇÃO CIENTÍFICA E INTELLECTUAL DA UNICAMP

**Versão do arquivo anexado / Version of attached file:**

Versão do Editor / Published Version

**Mais informações no site da editora / Further information on publisher's website:**

Sem URL

**DOI: 0**

**Direitos autorais / Publisher's copyright statement:**

©2024 by Elsevier. All rights reserved.

DIRETORIA DE TRATAMENTO DA INFORMAÇÃO

Cidade Universitária Zeferino Vaz Barão Geraldo

CEP 13083-970 – Campinas SP

Fone: (19) 3521-6493

<http://www.repositorio.unicamp.br>

**Design of a Ti-Zr-Fe-Ni medium entropy alloy for hydrogen storage at room temperature  
by thermodynamic calculations and semi-empirical descriptors**

Gaspar Andrade<sup>1</sup>, Payam Edalati<sup>1</sup>, Shivam Dangwal<sup>2</sup>, Kaveh Edalati<sup>2</sup>, Ricardo Floriano\*<sup>3</sup>

<sup>1</sup>Postgraduate Program in Mechanical Engineering, School of Mechanical Engineering,  
University of Campinas (FEM-UNICAMP), 200 Mendeleev St., Barão Geraldo, 13083-860,  
Campinas, São Paulo, Brazil

<sup>2</sup>WPI, International Institute for Carbon-Neutral Energy Research (WPI-I2CNER), Kyushu  
University, Fukuoka 819-0395, Japan

<sup>3</sup>School of Applied Sciences, University of Campinas (FCA-UNICAMP), Pedro Zaccaria, 1300,  
13484-350, Limeira, Brazil

**Corresponding author:** Ricardo Floriano

[rflorian@unicamp.br](mailto:rflorian@unicamp.br)

## ABSTRACT

This study employs the mechanisms that rule the hydrogen storage properties, especially the influence of compositional and microstructural factors on thermodynamics and kinetics, to design a medium-entropy alloy derived from the Ti-Zr-Fe-Ni system. A novel non-equiatomic alloy ( $\text{Ti}_{21}\text{Zr}_{21}\text{Fe}_{41}\text{Ni}_{17}$ ) was designed by applying semi-empirical models and computational thermodynamic calculations using the CALPHAD method. Four criteria were followed for design: valence electron concentration  $\text{VEC} = 6.2\text{-}6.5$ , atomic size mismatch  $\delta \geq 9.7\%$ , atomic radius ratio of hydride-forming to non-hydride forming element  $r_A/r_B = 1.149\text{-}1.219$ , and the C14 Laves structure stability as the major phase. The designated material was synthesized by casting and structural analysis showed that the alloy crystallizes as a major C14 phase (92.8 wt%) and a minor BCC phase. Transmission electron microscopy showed the presence of nanograins with a strong tendency to form coherent boundaries between the C14 grains and the interphase of C14 and BCC grains. The alloy showed very fast kinetics after a simple thermal activation and reversibly absorbed 1.4 wt% of hydrogen with a relatively small hysteresis between the cycles. For the kinetics properties, it was suggested that the hydride phase nucleates preferably in coherent grain boundaries resulting in the fast hydrogenation of the alloy. For thermodynamic properties, chemical composition designed by the four mentioned criteria should be considered, while iron also plays a critical role. The high atomic percentage of iron (41%) – a non-hydride forming element – stabilizes the C14 phase because of the elevated absolute contribution of the interaction parameter ( $\Omega_{ij}$ ) of the pair Fe-Zr, ( $\Omega_{ij} = -118.4$  kJ/mol), which results in a negative enthalpy of the mixture, with the C14 structure.

**Keywords:** Metal hydrides; Medium-entropy hydrides; Solid-state hydrogen storage;

## Introduction

High Entropy Alloys (HEAs) are known as a new class of materials with remarkable structural and functional properties <sup>1-4</sup>. Several attempts to propose a definition of HEAs have been made <sup>5</sup>. It is accepted that HEAs are composed of at least five principal elements mixed to produce a single-phase solid solution <sup>6</sup>. The mixing entropy ( $\Delta S_{\text{mix}}$ ) is the thermodynamic quantity generally used to classify the multi-principal element alloys. In this sense, HEAs usually fit in the interval where  $\Delta S_{\text{mix}} > 1.5R$  ( $R$ : universal gas constant). Medium-entropy alloys (MEAs) are classified when  $R < \Delta S_{\text{mix}} < 1.5R$ . Finally, the low-entropy alloys (LEAs) are considered when  $\Delta S_{\text{mix}} \leq R$  <sup>7</sup>. HEAs and MEAs are sometimes classified as multicomponent alloys <sup>8</sup>.

Since the beginning of the last decade, HEAs have been explored as potential materials for solid-state hydrogen storage <sup>9-12</sup>. Most of the hydrogen storage materials based on HEAs investigated so far fall within the category of solid solution alloys, incorporating elements with strong attraction to hydrogen, such as Ti, Zr, Nb, Hf, Ta, and V <sup>13-15</sup>. These alloys create highly stable hydrides that require inconveniently high temperatures, exceeding 400 °C, for the release of hydrogen. This characteristic restricts the practical application of these HEAs and their hydrides <sup>16-19</sup>.

In the field of hydrogen storage, a key challenge lies in discovering a material or hydride that can meet several criteria simultaneously. These include essential factors such as the ability to efficiently absorb and release hydrogen at room temperature in a reversible way, fast kinetics, easy activation, long-term cycling stability, suitable storage at a pressure close to atmospheric level, and high gravimetric capacity <sup>20-28</sup>. Given the significant impact of alloy composition on these hydrogen storage properties, HEAs offer an expansive compositional space to explore, presenting boundless opportunities to tailor these properties <sup>29-31</sup>.

The extensive compositional features of HEAs have been partly investigated using various methods rooted in thermodynamics. These methods encompass semi-empirical rules/descriptors, *ab initio* calculations, and the CALPHAD (Calculation of Phase Diagrams) approach<sup>32</sup>. These methods have a high potential for a deeper fundamental understanding of the phases existing within the HEAs system, their stability, and their correlation with specific desired attributes for hydrogen storage properties<sup>33-35</sup>. For example, valence electron concentration (VEC) has been correlated to hydrogen storage properties, and VEC = 6.4 was suggested to be favorable for low-temperature hydrogen absorption with good capacities and almost full reversibility<sup>36</sup>.

The stability of constituent phases within HEAs stands as a critical matter because of its strong impact on the hydrogen storage properties<sup>37-39</sup>. It was demonstrated that single-phase HEAs can be formed under specific combinations of mixing enthalpies ( $\Delta H_{\text{mix}}$ ), atomic size mismatches ( $\delta$ ), electronegativity mismatches ( $\Delta\chi$ ), and VEC<sup>40</sup>. These parameters vary between solid solution alloys and intermetallic compounds, where a solid solution usually forms for  $\delta \leq 6.6\%$ <sup>36</sup>. Another important parameter is the ratio of atomic radii between A and B components, where A indicates high hydrogen affinity elements and B indicates low hydrogen affinity elements. It was established that when the atomic radius ratio of hydride-forming to non-hydride-forming element  $r_A/r_B > 1.116$ , multicomponent alloys form multiphase or amorphous structures rather than single-phase crystalline structures<sup>41</sup>.

In a recent study by Ponsoni et al.<sup>42</sup>, they explored the influence of VEC,  $r_A/r_B$ , and  $\delta$  assisted by the CALPHAD method on the phase stability of AB<sub>2</sub>-type alloys (A: Ti, Zr, Nb; B=V, Cr, Mn, Fe, Co, Ni, Cu, and Zn) concerning their potential applications as hydrogen storage materials. A total of 1208 compositions (854 equiatomic and 354 non-equiatomic) were evaluated by phase stability. All 354 non-equiatomic alloys and 86 equiatomic compositions were predicted to form the C14

Laves phase. The high incidence of C14 was found for  $5.8 \leq \text{VEC} \leq 7.0$  and  $1.123 \leq r_A/r_B \leq 1.223$ . For  $\delta$ , the values were always higher than 5.0% for the Laves phase formation. Later studies also explored not only AB<sub>2</sub>-type alloys but also other stoichiometries starting from these elements <sup>43</sup>. Despite these studies, the hydrogen storage properties of these alloys and affecting factors for the design remain an open question.

In an attempt to select an intermetallic C14 Laves phase based on HEAs operating at room temperature, the current authors proposed three criteria: (i) AB<sub>2</sub>-type configuration, (ii) C14 Laves single-phase structure, and (iii) VEC of 6.4. Using the previous approach, an AB<sub>2</sub>-type HEA TiZrCrMnFeNi alloy was designed, which exhibited 1.7 wt% hydrogen absorption at room temperature <sup>44</sup>. Later, using first-principles calculations it was shown that the reason for the effectiveness of these criteria lay in the low hydrogen binding energy for room-temperature hydrogen storage <sup>43</sup>, which was also experimentally confirmed in a study about Zr-based HEAs <sup>45</sup>. These criteria were also generalized to other stoichiometries to select C14-based HEA such as TiZrNbFeCrNi <sup>46</sup>, TiZrNbCrFe <sup>47</sup>, and TiZrNbFeNi <sup>48</sup>. These alloys showed a major C14 Laves phase with a small amount of BCC phase. It was confirmed that when VEC is set to values near 6.4, the alloys could reversibly absorb hydrogen with a simple activation process, mostly at room temperature with fast kinetics <sup>43-48</sup>. Although all these studies paid attention to the entropy of mixing due to a large number of principal elements, the enthalpy of mixing is an important parameter in MEAs that was not considered in these studies. It is then necessary to go deeper into the role of  $\Delta H_{\text{mix}}$  on the stabilization of the Laves phases-based MEAs. Moreover, despite some recent progress <sup>49</sup>, the significance of secondary phases in C14-based alloys and their influence on the nucleation of the hydride is still an open issue. An understanding of these issues can facilitate the design of multicomponent alloys for hydrogen storage.

In this study, by considering the influence of compositional and microstructural factors we propose a new design strategy for MEAs for hydrogen storage in a model Ti-Zr-Fe-Ni system. The designed alloy –  $\text{Ti}_{21}\text{Zr}_{21}\text{Fe}_{41}\text{Ni}_{17}$  – was selected by applying both computational thermodynamic calculations using CALPHAD and semi-empirical descriptors to obtain C14 Laves as the major phase. The alloy was produced by arc melting under an argon atmosphere and studied by detailed structural and microstructural characterizations via X-ray diffraction (XRD), scanning electron microscopy (SEM), and transmission electron microscopy (TEM). Hydrogen storage properties at room temperature were also systematically investigated, and the correlations between secondary phase and hydrogen storage properties were discussed.

## **Material and methods**

To select new MEAs for room-temperature hydrogen storage, a semi-empirical and thermodynamics-based method was applied. Firstly, hydride-forming elements A (Zr, Ti, Nb, and V) and non-hydride-forming elements B (Cr, Mn, Fe, Ni, and Co) were selected to combine in some different stoichiometries such as AB,  $\text{AB}_2$ ,  $\text{AB}_{1.5}$ , and  $\text{A}_{1.5}\text{B}$ , resulting in a total of 230 possible compositions. In the second step, some restrictions were applied to obtain compositions with a high tendency to form the C14 Laves phase, in the following order:  $\text{VEC} = 6.2\text{-}6.5$ ,  $\delta \geq 9.7\%$ , and  $r_A/r_B = 1.149\text{-}1.219$ . The VEC was calculated with the weighted average of the VEC of each element in the alloy, considering their stoichiometry. For the atomic size mismatch ( $\delta$ ), it was taken into account the standard deviation of the atomic radius of the elements of the alloy. Finally, the  $r_A/r_B$  was calculated as the ratio between the average atomic radius of the elements positioned in the A sites and B sites of the C14 unit cell.

The selection resulted in 20 original alloy compositions. These alloys were carefully evaluated by the CALPHAD method using Thermocalc to check the stability of phases during the thermodynamic equilibrium and to confirm the high trend to the formation of the C14 Laves phase. Following these procedures,  $\text{Ti}_{21}\text{Zr}_{21}\text{Fe}_{41}\text{Ni}_{17}$  MEA was chosen as the object of this study, to determine its hydrogen storage properties.

The alloy was experimentally prepared through arc melting of high-purity elemental powders of Zr (99.5%), Ti (99.99%), Fe (99.97%), and Ni (99.99%). The process of arc melting was executed utilizing a non-consumable tungsten electrode and a water-cooled copper crucible under a high-purity argon atmosphere. To enhance chemical uniformity, the ingots underwent six rotations and remelting cycles, while the mass loss was negligible. Subsequently, the ingots were cut into smaller pellets for further microstructural characterization and hydrogen storage measurements.

For crystal structure analysis, the alloy was crushed into micro-sized powders and subjected to XRD measurements. The XRD analysis utilized a Cu-K $\alpha$  radiation source ( $\lambda = 0.15406$  nm) with an X'Pert Panalytical diffractometer operating at 45 kV and 40 mA. The Rietveld refinement method, in conjunction with GSAS-II software, was employed to determine the lattice parameters, phase fractions (wt%), crystallite size, and isotropic microstrain. The refinement process included adjusting background estimation using a Chebyshev background function with five coefficients, determining phase fractions, and refining lattice parameters. The resulting refinements demonstrated residual values (Rwp) and goodness-of-fit (GOF) below 5%, affirming the high quality and reliability of the results<sup>50</sup>.

Microstructural investigations were conducted using SEM and high-resolution TEM. For SEM, the samples underwent mechanical polishing with colloidal silica of 60 nm particle size. The polished samples were examined using a Philips XL-30 FEG SEM equipped with energy-

dispersive X-ray spectroscopy (EDS). Back-scattered electron and secondary electron (BSE and SE) images, along with elemental mapping at different magnifications in selected regions, were captured for all samples. For TEM analysis, ethanol was used as a medium to crush the alloy while preventing oxidation. After being crushed, the sample was dispersed onto a carbon grid and immediately examined by TEM.

To assess hydrogen storage performance, pressure-composition-temperature (PCT) absorption and desorption isotherms, along with kinetic measurements under a hydrogen pressure of 3.5 MPa, were carried out at room temperature by using a Sieverts-type machine. Samples weighing approximately 250 mg were crushed in air followed by passing the crushed powders through a sieve of 75  $\mu\text{m}$  size.

The hydrogenation measurements were first conducted without any activation treatment, but since the alloys did not absorb hydrogen, an activation procedure was applied. The activation procedure applied consisted of increasing the temperature to 450 °C for 3h under a dynamic vacuum **and left to cool down to room temperature by itself**. It is important to mention that the activation procedure does not lead to any structural phase transitions, due to the small temperature compared to the melting point of the alloys. Selected samples were examined by XRD after hydrogenation, and in this case, the samples were examined by XRD in less than 5 min after their removal from the reactor of the Sieverts machine.

## Results

**Fig. 1** shows the phase diagram of the designed alloy determined by Thermocalc. The thermodynamic computational calculation indicates that the alloy crystallizes with the majority of

the C14 phase in the equilibrium. Furthermore, considering the large solidification interval, the C14 phase remains stable in the liquid phase and grows at elevated temperatures (1800 °C) until its complete solidification. Although the thermodynamic equilibrium foresees other phases such as BCC in temperatures below 750 °C, their fractions are very low, under 10% of all phases.

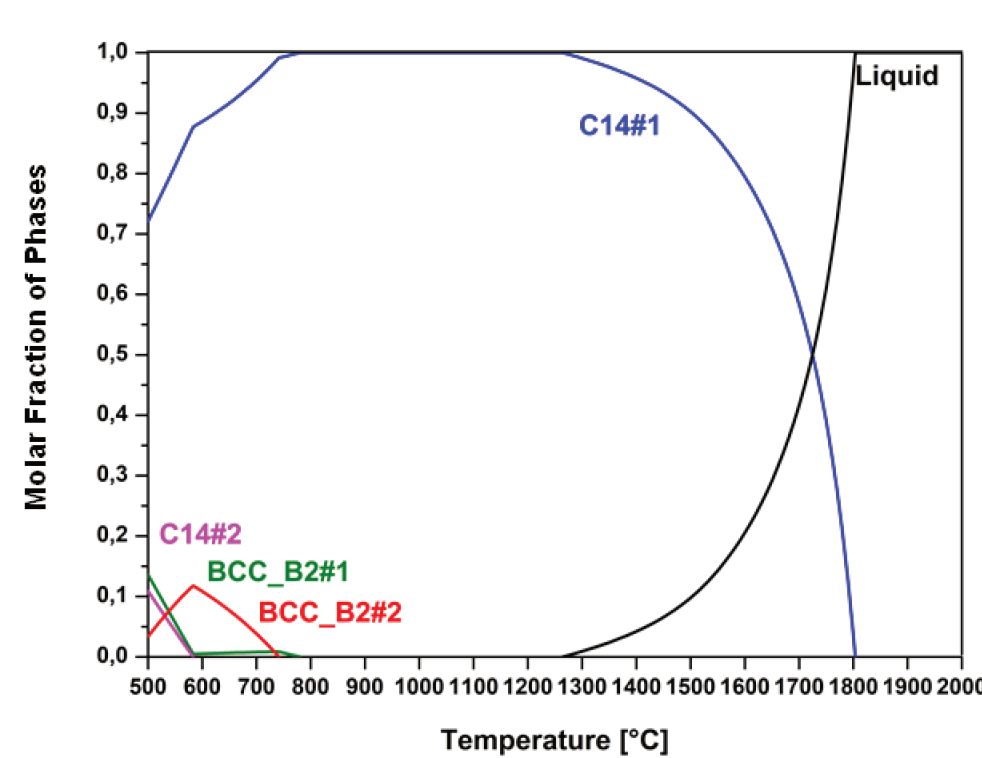


**Figure 1:** Molar fraction of equilibrium phases as a function of temperature calculated for the  $\text{Ti}_{21}\text{Zr}_{21}\text{Fe}_{41}\text{Ni}_{17}$  alloy using CALPHAD and TCHEA3 database.

**Table 1** shows the atomic fraction of each element in the C14 phase of the referred composition, determined by CALPHAD. The occupation factor of each element in the C14 unit cell was used later to determine the structural parameters by the Rietveld refinement.

**Table 1 – Structural parameters of the C14 unit cell in  $Ti_{21}Zr_{21}Fe_{41}Ni_{17}$  alloy.**

Phase	Atom	Wyckoff position	Molar fraction	Occupation factor
C14	Zr	4f (1/3, 2/3, 0.06030)	0.21	0.62
	Ti		0.21	0.38
Space Group: P63/mmc (194)	Fe	2a (0, 0, 0)	0.41	0.61
	Ni		0.17	0.26
	Ti		-----	0.13
	Fe	6h (0.83170, 0.66340, 1/4)	-----	0.61
	Ni		-----	0.26
	Ti		-----	0.13

**Fig. 2** and **Fig. 3** show the XRD patterns with the corresponding Rietveld refinement and the SEM/EDS images of the  $Ti_{21}Zr_{21}Fe_{41}Ni_{17}$  alloy, respectively. The Rietveld refinement was done by using the crystal structure data displayed in **Table 1** which was built by using the information of the composition and the constitution of the calculated C14 Laves phase at 1000 °C. The agreement indices for the refinement are GOF = 1.45 and Rwp = 3.022. The structural parameters of the C14 phase, as determined by Rietveld, are  $a = 4.968 \text{ \AA}$  and  $c = 8.079 \text{ \AA}$ . The Rietveld refinement indicates that the alloy crystallizes as a major C14 phase – 92.8 wt% – and a minor BCC phase – 7.2 wt%, in good agreement with the calculated phase diagram in **Fig. 1**. These results agree with the SEM images shown in **Fig. 3-a** and **Fig. 3-b**, where it is evident the existence

of a two-phase microstructure. The elemental mappings shown in **Fig. 3** suggest that some elements tend to occupy one phase instead of another. For example, a higher concentration of Ni and Ti in the dark regions detached in **Fig. 3-b** is observed, while at the same time, these areas are poor in Fe. On the other hand, Zr is very well distributed in the whole microstructure, meaning that this element is present in both C14 and BCC phases. It should be also noted in the EDS spectra taken from the whole area in **Fig. 3-c** that the atomic fraction of each element is very close to the nominal percentage of these elements in the referred alloy.

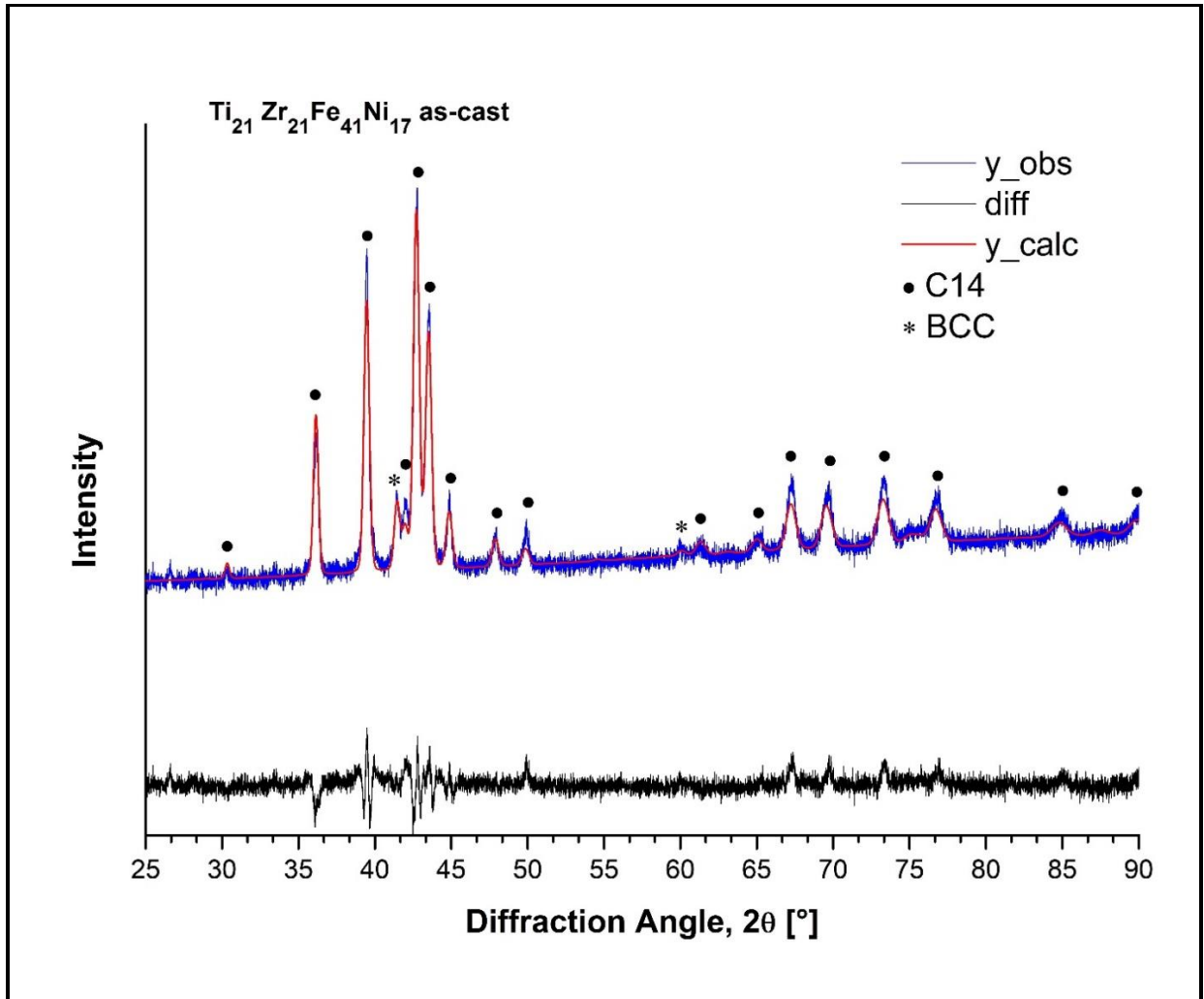


**Figure 2:** XRD pattern and Rietveld refinement of the  $\text{Ti}_{21}\text{Zr}_{21}\text{Fe}_{41}\text{Ni}_{17}$  alloy in the as-cast condition.

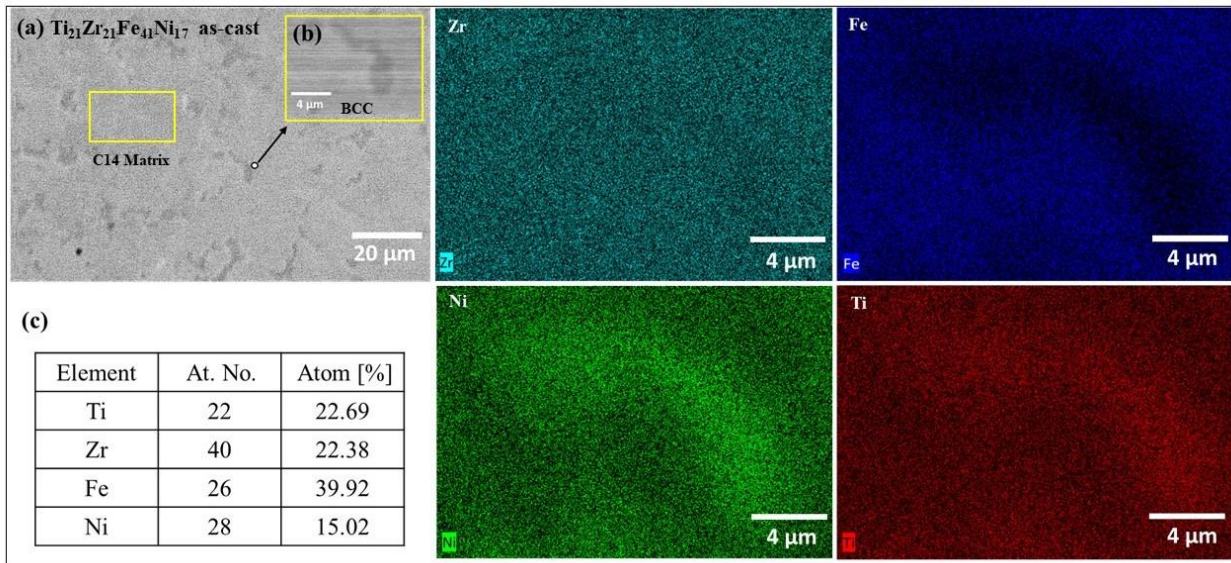


**Figure 3:** SEM images and corresponding EDS elemental mappings of  $Ti_{21}Zr_{21}Fe_{41}Ni_{17}$  alloy in the as-cast condition. **a)** SEM images using BSE mode, **b)** magnified view of BSE image, **c)** EDS maps and quantification of the selected BSE area in (b).

**Fig. 4** shows TEM images: **a)** bright field (BF), **b)** SAED pattern, and **c)** dark field (DF) of the  $Ti_{21}Zr_{21}Fe_{41}Ni_{17}$  alloy in the as-cast state. The DF image was taken from the location of the diffracted rays indicated by the yellow arrow in the SAED pattern. The High-resolution TEM image in **Fig. 4-d** shows some nanograins, where the crystal directions are indexed using the fast Fourier transform (FFT) analysis. As can be seen, both BCC and C14 Laves phases are crystallized next to each other in this type of grain. **Fig. 4-e** and **Fig. 4-f** show the two grain boundaries selected with yellow squares in a higher magnification. **Fig. 4-g** shows one of these larger grains that contains a dislocation. **Fig. 4-h**, prepared using the Inverse FFT technique from the yellow square area, clearly shows the existence of this dislocation.

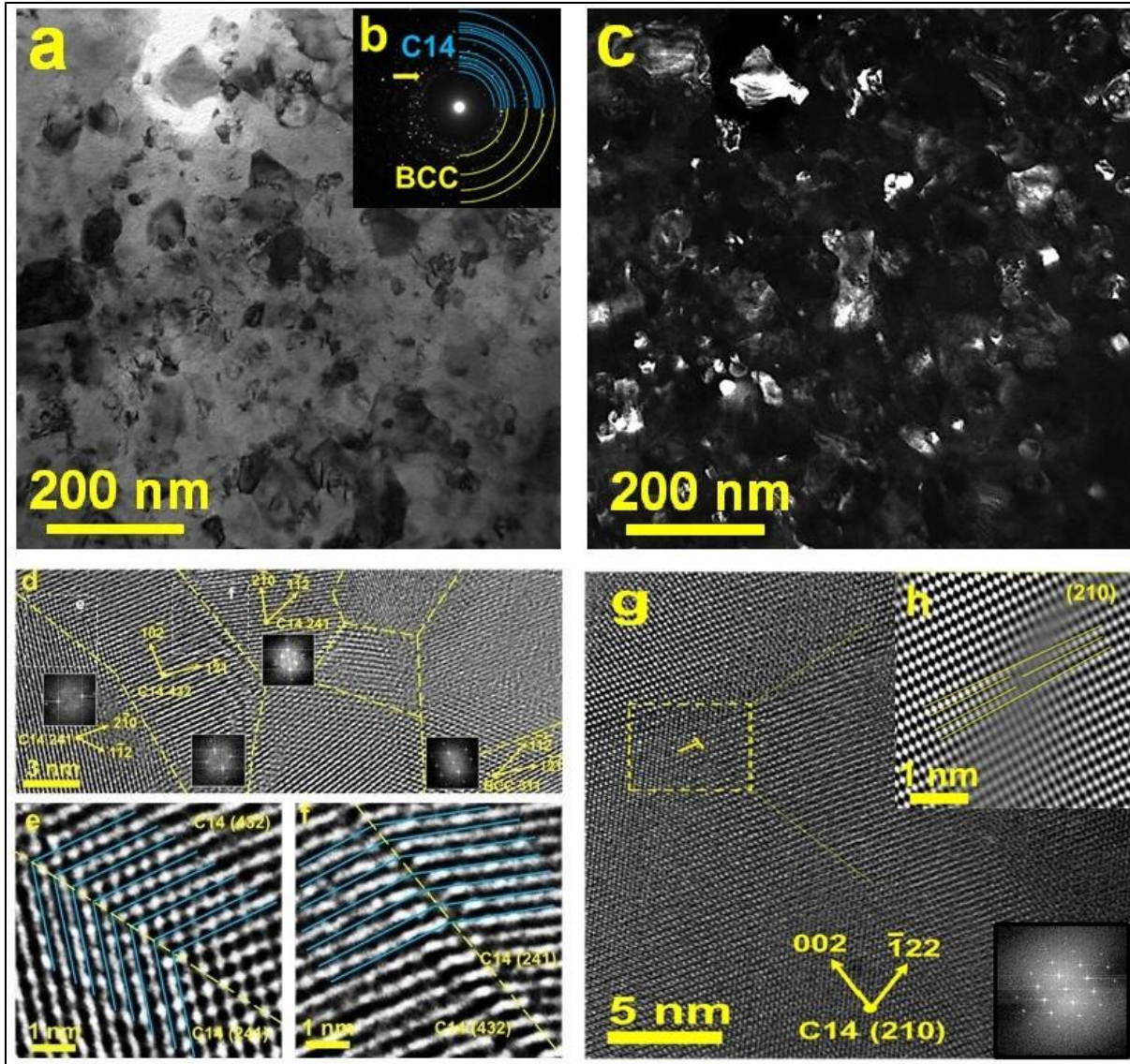


**Figure 4:** TEM images of the  $\text{Ti}_{21}\text{Zr}_{21}\text{Fe}_{41}\text{Ni}_{17}$  alloy in the as-cast state. **a)** BF image, **b)** SAED pattern, **c)** DF image, **d)** high-resolution image showing nanoscale C14 and BCC grains, **e-f)** lattice images showing coherent grain boundaries, **g-h)** high-resolution image and corresponding inverse FFT analysis showing dislocations in large grains.

Regarding the hydrogen absorption properties, the PCT isotherm measurements were conducted for the  $\text{Ti}_{21}\text{Zr}_{21}\text{Fe}_{41}\text{Ni}_{17}$  alloy in the as-cast state at room temperature without any activation

procedure. The sample did not show any absorption ability in this condition, and thus, the activation procedure at 450 °C for 3h under dynamic vacuum was applied. **Fig. 5** shows the 4<sup>th</sup> PCT absorption and desorption isotherms of the  $\text{Ti}_{21}\text{Zr}_{21}\text{Fe}_{41}\text{Ni}_{17}$  alloy at room temperature after the activation procedure. Firstly, by looking at all PCT absorption and desorption isotherms, the absence of a well-defined equilibrium plateau pressure is evident. Secondly, the alloy starts to absorb hydrogen at very low pressure, of the order of kilopascal, in the first absorption. The alloy absorbs 1.4 wt% of hydrogen (subtracted from the initial 0.2 wt%) and showed a very good reversibility at room temperature desorbing almost the same amount of hydrogen in all cycles.

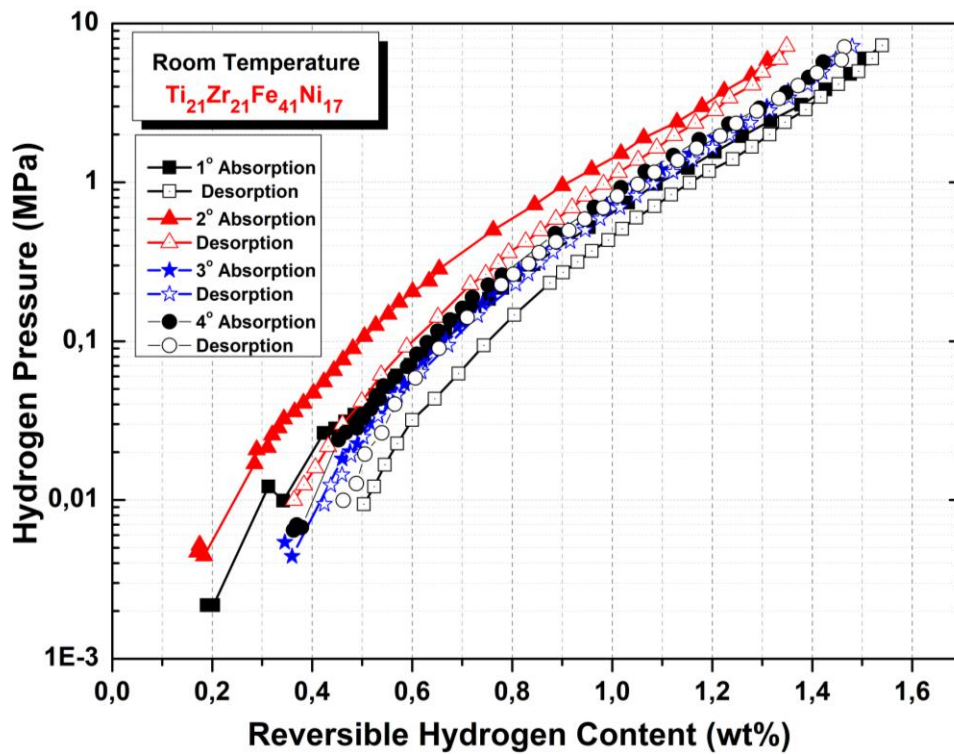


**Figure 5:** PCT absorption/desorption isotherms at room temperature for  $\text{Ti}_{21}\text{Zr}_{21}\text{Fe}_{41}\text{Ni}_{17}$  alloy after activation.

Additionally, it's noteworthy that there's a slight shift in the position of the curves along the 'x' axis observed in the PCT curves. This shift is attributed to the decline in hydrogen capacity throughout the PCI cycles, a trend also observed during the kinetic cycling discussed ahead.

**Fig. 6-a** shows the absorption kinetics of  $\text{Ti}_{21}\text{Zr}_{21}\text{Fe}_{41}\text{Ni}_{17}$  alloy at room temperature under a hydrogen pressure of 3.5 MPa after PCT isotherm measurements. As can be shown, the alloy exhibits a very fast absorption kinetics without any incubation time and achieves the maximum capacity of 1.4 wt% of hydrogen after 60 seconds. The cycling test applied to this alloy, as highlighted in **Fig. 6-b**, reveals that the hydrogen storage capacity is quite stable after ten cycles. The maximum capacity of 1.17 wt% remains stable between the 2<sup>nd</sup> and the 10<sup>th</sup> cycles, while a small drop in the capacity can be noticed between the 1<sup>st</sup> to the 2<sup>nd</sup> cycles.

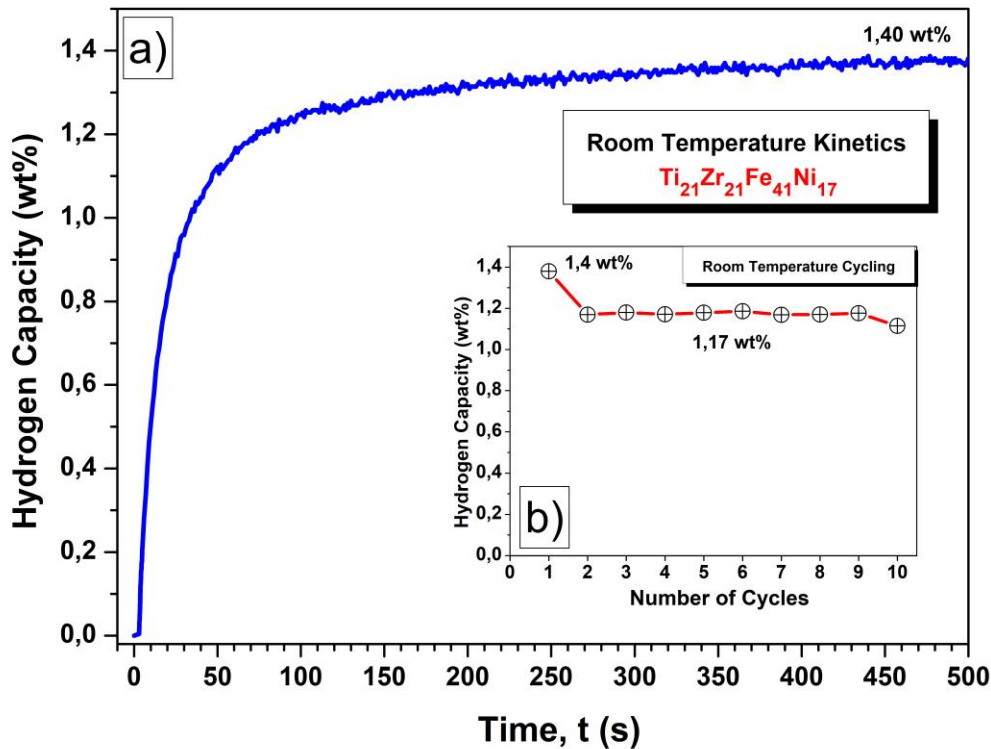


**Figure 6:** a) Kinetic curve of  $\text{Ti}_{21}\text{Zr}_{21}\text{Fe}_{41}\text{Ni}_{17}$  alloy at room temperature under the hydrogen pressure of 3.5 MPa, b) the hydrogen storage capacity as a function of the number of cycles.

The crystal structure of the alloy after hydrogenation was also checked. For comparison, **Fig. 7** shows the XRD patterns and the indexed phases of the alloy in the as-cast state and after hydrogenation. As seen in the image, there is no shift in the angular positions of the C14 peaks after hydrogenation compared to the as-cast sample, which means that the alloy immediately releases hydrogen when exposed to atmospheric pressure, even considering the short time between its removal from the reactor and the XRD analysis. The cell parameters for the C14 after spontaneous desorption are  $a = 4.979 \text{ \AA}$  and  $c = 8.096 \text{ \AA}$ , which are very close to the cell

parameters obtained for the as-cast sample. In addition to the detection of the C14 phase, the presence of the BCC phase is also noticed, in agreement with **Fig. 2**.

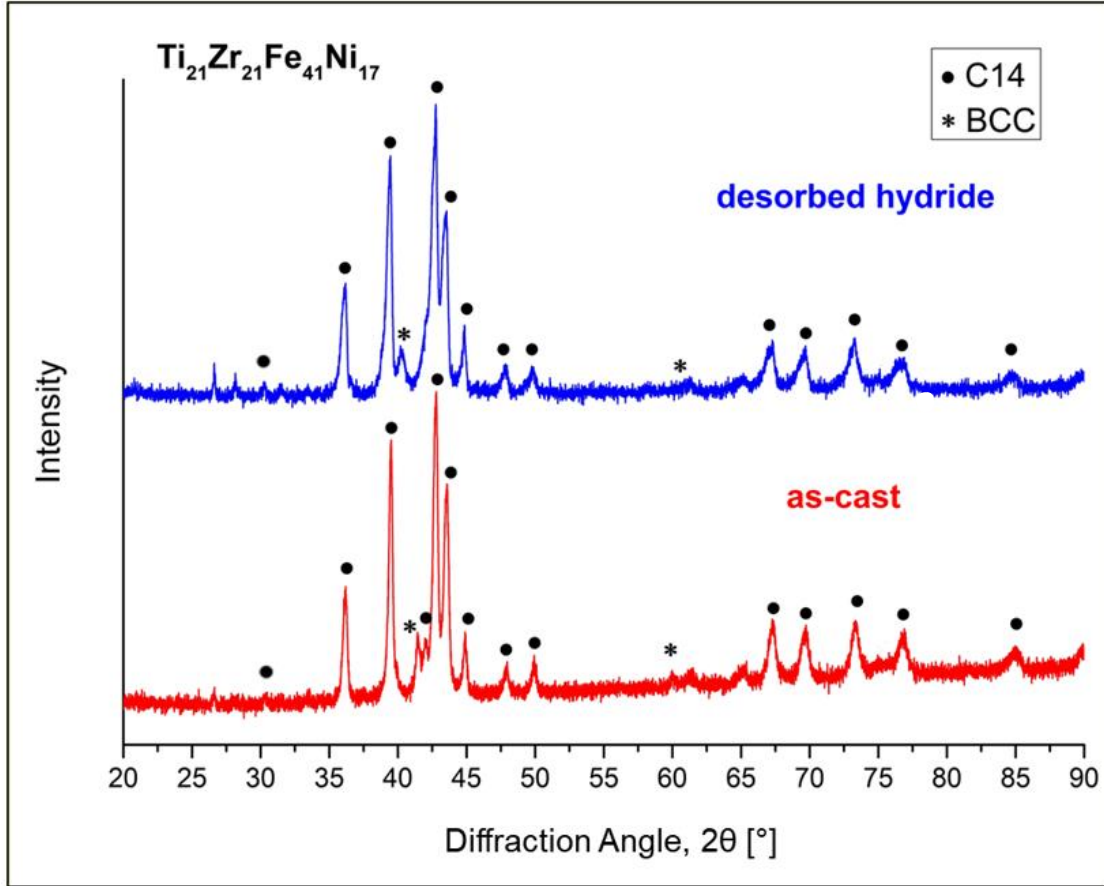


**Figure 7:** XRD patterns of  $Ti_{21}Zr_{21}Fe_{41}Ni_{17}$  alloy in the as-cast and hydrogenated states. Bragg angle positions for C14 and BCC phases were also included as references.

## Discussion

Intermetallic HEAs having the C14 Laves structure as the major phase demonstrated a great ability to absorb and desorb hydrogen at low temperatures<sup>51</sup>, with easy activation<sup>44</sup>. However, studies on MEAs, in which entropy is lower and the enthalpy is more dominant, for hydrogen storage at room temperature are limited. In this study, we applied the combination of semi-empirical descriptors followed by the CALPHAD thermodynamic calculations to design MEAs for hydrogen storage. The results concerning the crystal structure initially predicted using the CALPHAD

method (**Fig. 1**) and subsequently by the XRD (**Fig. 2**), confirmed that the proposed design method correctly selected a  $\text{Ti}_{21}\text{Zr}_{21}\text{Fe}_{41}\text{Ni}_{17}$  alloy with a high tendency to form the majority of the C14 Laves phase **stable in the thermodynamic equilibrium**. In this section, some structural and microstructural features of the designated alloy and their influence on hydrogen storage properties need to be discussed.

The microstructural analysis represented by the SEM images (**Fig. 3**) showed the appearance of two distinct regions: dark and gray regions. The dark regions refer to the Ti- and Ni-rich regions, which are expected for the composition of the BCC phase according to the CALPHAD prediction. Moreover, the apparent amount of the BCC phase is compatible with the quantity of this phase as determined by the Rietveld refinement. On the other hand, the gray regions that appear in high proportion in the SEM images are associated with the C14 phase. The absence of Fe in the BCC phase and its abundant presence in the C14 Laves phases is noted in EDS analysis. As we will explain later, Fe is responsible for decreasing the enthalpy of the mixture, favoring the crystallization of intermetallic phases, such as the C14 phase.

From the TEM analysis (**Fig. 4**), it can be seen that the grains have crystallized in various sizes ranging from micrometers to nanometers, which is a little abnormal for the sample after casting. **One explanation remains on the possible small solidification interval of the alloy. The C14 phase nucleates with a small amount of free energy, right before the end of the liquidus line. In this case, the undercooling provided by the water-cooled crucible during arc melting causes a high rate of nucleation, preventing the grains from growing**<sup>52</sup>. The SAED analysis with a ring pattern (**Fig. 4-b**) clearly shows the existence of nanograins of two phases, BCC and C14-Laves, which is consistent with the prediction of thermodynamic simulation with the CALPHAD method and the results of XRD analysis. It is important to pay attention to the grain boundaries of these nanograins

because they show a strong tendency to form coherent grain boundaries with low energy. Unlike large grains, dislocations are not seen in nanograins, which is expected due to the instability of dislocations near grain boundaries.

The PCT cycles of absorption and desorption (**Fig. 5**) show that the alloy can reversibly absorb and desorb a reasonable amount of hydrogen with almost no hysteresis. It is worth pointing out that, the alloy became fully activated after a simple activation procedure as already described in the experimental section. The absence of a well-defined plateau in the PCT curves suggests the hydrogen atoms form a solid solution alongside the metallic atoms. Taking the pressure of 0.1 MPa (1 atm) as a reference line, most parts of the PCT curves are above this level of pressure. This is desirable for hydrogen storage applications because the formed hydride is not so stable, being able to desorb hydrogen at atmospheric pressure. In terms of kinetics (**Fig. 6**), the selected alloy showed a very fast hydrogen absorption after a simple thermal activation step. The maximum amount absorbed of 1.4 wt.% of hydrogen is comparable with other C14-based alloys already reported in the literature. The TiZrNbCrFe<sup>47</sup> alloy was able to absorb 1.35 wt.% at room temperature, while the TiZrNbFeNi<sup>48</sup> absorbed 1.2 wt.% at room temperature, after the same heat treatment activation of 450 °C for 3 hours in a vacuum. Also, the maximum amount of hydrogen remains almost the same after the second cycle. This feature can be attributed to the stability of the C14 phase under hydrogenation/dehydrogenation, since the reaction occurs in a single step, without any intermediate hydride phase<sup>53</sup>.

From the thermodynamic point of view, the reversibility of the alloy can be associated with the calculated value of VEC = 6.5. It was proposed that VEC should be kept around 6.4 to improve the hydrogen storage properties<sup>44,47-48</sup>. Also, the calculated enthalpy of mixture ( $\Delta H_{\text{mix}}$ ) for the Ti<sub>21</sub>Zr<sub>21</sub>Fe<sub>41</sub>Ni<sub>17</sub> alloy is equal to -29 kJ/mol. The Laves phases-based HEAs with  $\Delta H_{\text{mix}}$  of -15 to

-5 kJ/mol are usually considered suitable candidates for hydrogen storage applications as they demonstrate high hydrogen-to-metal (H/M) ratios and favourability for hydride formation enthalpy ( $\Delta H_{\text{form}}$ )<sup>54,55</sup>. A very negative enthalpy of formation such as -29 kJ/mol means that the metallic bonds are strong, and as explained by the Miedema rule, a very stable intermetallic compound (strong metallic bonds) forms an unstable hydride<sup>56</sup>. It should be noted that the strong negative  $\Delta H_{\text{mix}}$  calculated for this alloy with high Fe content (41 at%) comes from the elevated contribution of the interaction parameter ( $\Omega_{ij}$ ) of the pair Fe-Zr, where  $\Omega_{ij} = -118.4$  kJ/mol. The interaction parameters of Zr-Ni (-236.4 kJ/mol) and Ti-Ni (-124.1 kJ/mol) are also significant, but the small atomic percentage of Ni in the alloy tends to decrease its contribution to the final value of the mixing enthalpy. The other contributions are too small, as follows for the Zr-Ti (-0.8 kJ/mol), Fe-Ti (-61.6 kJ/mol), and Fe-Ni (-6.4 kJ/mol). Moreover, since the  $\text{Ti}_{21}\text{Zr}_{21}\text{Fe}_{41}\text{Ni}_{17}$  alloy can be classified as a MEA ( $\Delta S_{\text{mix}} = 8.3$  J/mol. K which is lower than  $1.5R$ , where  $R = 8.31$  J/mol. K), the strong negative  $\Delta H_{\text{mix}}$  plays the main role in stabilizing the intermetallic C14 phase. Taking all together, the high concentration of Fe – a non-hydride forming element – is responsible not just for the good reversibility of the alloy, but also for the stabilization of the C14 phase, which grants good hydrogen absorption properties.

Regarding the mechanisms that could explain the attractive hydrogen storage properties of the  $\text{Ti}_{21}\text{Zr}_{21}\text{Fe}_{41}\text{Ni}_{17}$  alloy, three main reasons are presented here: i) appropriate thermodynamics of the system which was adjusted by semi-empirical descriptors and thermodynamic calculations, ii) the presence of interphase boundaries; and iii) the presence of coherent grain boundaries. In a recent study<sup>57</sup>, it was suggested that the presence of a small amount of a second phase appears to be a good solution to the issue of the activation of some alloys<sup>58</sup>. This is supported by the fact that the interphase boundaries can act like a hydrogen transport medium, which explains the easy

activation of dual-phase alloys<sup>59</sup>. However, it was claimed that the presence of interphase boundaries is not the only mechanism that explains the easy activation in HEAs, because they also can amplify the heterogeneous nucleation of the hydride at grain boundaries. The TEM images showed the presence of nanograins with a strong tendency to form coherent grain boundaries between the C14 grains. A close look at **Fig. 4-d** shows that even some C14/BCC interphase boundaries are coherent. The nucleation of the hydride can be favored due to the reduction of energy of the grain boundaries, which explains the fast kinetics and good reversibility of the alloy. Moreover, the presence of nanoscale grains in large quantities means more grain boundaries than expected for large grains, acting as a pathway for hydrogen transport from the surface to the bulk. Even though low-angle coherent grain boundaries are less favorable to nucleate the hydride phase than high-angle grain boundaries, some studies<sup>60-61</sup> demonstrated that coherent grain boundaries are more favorable to promote the diffusion of hydrogen atoms to the bulk, because of their highly symmetrical interstitial positions.

## Conclusions

This study reported the hydrogen storage properties of an original  $\text{Ti}_{21}\text{Zr}_{21}\text{Fe}_{41}\text{Ni}_{17}$  MEA, designed by theoretical thermodynamic calculations and semi-empirical descriptors (valence electron concentration, atomic size mismatch, and atomic radius ratio of hydride-forming to non-hydride forming element) was investigated. The alloy showed fast kinetics and could reversibly absorb 1.4 wt.% of hydrogen at room temperature with a relatively small hysteresis along the cycles. The structural measurements by the Rietveld refinement show the alloy crystallizes as 92.8% of the C14 phase and a minor amount of the BCC phase, in agreement with the phase diagram obtained by the thermodynamic calculations. Additionally, nanoscale grains were observed with coherent

interphase grain boundaries. It was proposed that the hydride phase nucleates preferably in coherent grain boundaries, which explains the fast kinetics of the alloy. The applied empirical descriptors and thermodynamic computational calculations to select the C14-based alloy in this study can be principally used to design other MEAs from other systems for hydrogen storage.

### **Conflicts of interest**

There are no conflicts to declare.

### **Acknowledgments**

This work is supported in part by a grant from the Brazilian Research Funding Agency FAPESP (Regular Project No. 2022/01351-0), and in part by Grants-in-Aid for Scientific Research on Innovative Areas from the MEXT, Japan (JP19H05176 & JP21H00150).

### **References**

- 1 B. Cantor, I.T.H. Chang, P. Knight and A.J. Vincent, *Materials Science Engineering*, 2004, 357-377, DOI: 10.1016/j.msea.2003.10.257.
- 2 Y. Ye, Q. Wang, J. Lu, C. Liu and Y. Yang, *Materials Today*, 2016, **19**, 349-62. DOI: 10.1016/j.mattod.2015.11.026.
- 3 D.B. Miracle and O.N. Senkov, *Acta Materialia*, 2017, **122**, 448-511, DOI: 10.1016/j.actamat.2016.08.081.
- 4 F. Marques, M. Balcerzak, F. Winkelmann, G. Zepon and M. Felderhoff, *Energy & Environmental Science*, 2021, DOI: 10.1039/d1ee01543e.
- 5 L. Luo, L. Chen, L. Li, S. Liu, Y. Li, C. Li, L. Li, J. Cui and Y. Li, *International Journal of Hydrogen Energy*, 2024, **50**, 406-430, DOI: 10.1016/j.ijhydene.2023.07.146.
- 6 T. R. Somo, M.V. Lototsky, V.A. Yartys, M.W. Davids and S.N. Nyamsi, *Journal of Energy Storage*, 2023, **73**, 108969, DOI: 10.1016/j.est.2023.108969.
- 7 K-F. Yao, H-W. Luan, Y. Shao, J-F. Li, W-L Mao, Z-D. Han and C. Shao, *Scripta Materialia*, 2020, 40-44, DOI: 10.1016/j.scriptamat.2019.12.041.
- 8 S. Akrami, P. Edalati, M. Fuji and K. Edalati, *Materials Science and Engineering*, 2021, **146**, 100644, DOI: 10.1016/j.mser.2021.100644.

- 9 I. Kuncce, M. Polanski and J. Bystrzycki, *International journal of hydrogen energy*, 2013, 12180-12189, DOI: 10.1016/j.ijhydene.2013.05.071.
- 10 Y. Wang, J. Yuan, J. Chen, Z. Li, H. Huang, Y. Lv, B. Liu, Y. Li and Y. Wu, *Scripta Materialia*, 2022, DOI: 10.1016/j.scriptamat.2022.114548.
- 11 S-K. Chen, P-H. Lee, H. Lee, H-T. Su, *Materials Chemistry and Physics*, 2018, 336-347 DOI: 10.1016/j.matchemphys.2017.08.008.
- 12 D.J.M. King, S.C. Middleburgh, A.G. Mcgregor and M.B Cortie, *Acta Materialia*, 2016, **104**, 172-179, DOI: 10.1016/j.actamat.2015.11.040.
- 13 X. Yang and Y. Zhang, *Materials Chemistry and Physics*, 2012, **132**, 233-238, DOI: 10.1016/j.matchemphys.2011.11.021.
- 14 K. Guruvadyathri, M. Vaidya and B.S. Murty, *Scripta Materialia*, 2020, **188**, 37-43, DOI: 10.1016/j.scriptamat.2020.06.060.
- 15 Y.F. Kao, S.K. Chen, J.H. Sheu, J.T. Lin, W.E. Lin, J.W. Yeh, S.J. Len, T.H. Liou and C.W. Wang, *International Journal of Hydrogen Energy*, 2010, **35**, 46-59, DOI: 10.1016/j.ijhydene.2010.06.012.
- 16 M.M. Nygård, G. Ek, D. Karlsson, M.H. Sørby, M. Sahlberg and B.C. Hauback, *Acta Materialia*, 2019, **175**, 121-129, DOI: 10.1016/j.actamat.2019.06.002.
- 17 M.M. Nygård, G. Ek, D. Karlsson, M.H. Sørby, M. Sahlberg and B.C. Hauback, *International Journal of Hydrogen Energy*, 2019, **44**, 29140-29149, DOI: 10.1016/j.ijhydene.2019.03.223.
- 18 M. Sahlberg, D. Karlsson, C. Zlotea and U. Jansson, *Scientific Reports*, 2016, **6**, DOI: 10.1038/srep36770.
- 19 C. Zhang, A. Song, Y. Yuan, Y. Wu, P. Zhang, Z. Lu, X. Song, *International Journal of Hydrogen Energy*, 2020, **45**, 5367-5374, DOI: 10.1016/j.ijhydene.2019.05.214.
- 20 C. Zlotea, M.A. Sow, G. Ek, J.P. Couzinié, L. Perrière, I. Guillot, J. Bourgon, K.T. Møller, T.R. Jensen, E. Akiba and M. Sahlberg, *Journal of Alloys and Compounds*, 2019, **775**, 667-674, DOI: 10.1016/j.jallcom.2018.10.108.
- 21 L. Chanchetti, S.M. Oviedo Diaz, D.H. Milanez, D.R. Leiva, L.I.L. De Faria and T.T. Ishikawa, *International Journal of Hydrogen Energy*, 2016, **41**, 18301-18310, DOI: 10.1016/j.ijhydene.2016.08.137.
- 22 M. Hirscher, V.A. Yartys, M. Baricco, J.B. Von Colbe, D. Blanchard, R.C. Bowman Jr, D.P. Broom, C.E. Buckley, F. Chang, P. Chen, Y.W. Cho, J-C. Crivello, F. Cuevas, W.I.F. David, P.E. De Jongh, R.V. Denys, M. Dornheim, M. Felderhoff, Y. Filinchuk, G.E. Froudakis, D.M. Grant, E.M.A. Gray, B.C Hauback, T. He, T.D. Humphries, T.R. Jensen, S. Kim, Y. Kojima, M. Latroche, H-W. Li, M.V. Lototsky, J.W. Makepeace, K.T. Møller, L. Naheed, P. Ngene, D. Noreus, M.M. Nygård, S. Orimo, M. Paskevicius, L. Pasquini, D.B. Ravnsbæk, M.V. Sofianos, T.J. Udovic, T. Vegge, G.S. Walker, C.J. Webb, C. Weidenthaler and C. Zlotea, *Journal of Alloys and Compounds*, 2020, **827**, DOI: 10.1016/j.jallcom.2019.153548.

- 23 J. Huot, F. Cuevas, S. Deledda, K. Edalati, Y. Filinchuk, T. Grosdidier, B.C. Hauback, M. Heere, T.R. Jensen, M. Latroche and S. Sartori, *Materials*, 2019, **12**, DOI:10.3390/ma12172778.
- 24 R. Cohen, K. West and J. Wernick, *Journal of Less-Common Metals*, 1980, **73**, 273-279. DOI: 10.1016/0022-5088(80)90315-X.
- 25 T. Maeda, T. Fuura, I. Matsumoto, Y. Kawakami and M. Masuda, *Journal of Alloys and Compounds*, 2013, **580**, 255-258, DOI: 10.1016/j.jallcom.2013.03.230.
- 26 X. Zhao, J. Zhou, X. Shen, M. Yang and L. Ma, *International Journal of Hydrogen Energy*, 2012, **37**, 5050-5055, DOI: 10.1016/j.ijhydene.2011.12.010.
- 27 L. Schlapbach and T. Riesterer, *Applied Physics A*, 1983, DOI: 10.1007/BF00820257.
- 28 M.O. De Marco, Y. Li, H-W Li, K. Edalati and R. Floriano, *Advanced Engineering Materials*, 2020, DOI: 10.1002/adem.201901079.
- 29 J. Liu, J. Xu, S. Sleiman, F. Ravalison, W. Zhu, H. Liu, H. Cheng and J. Huot, *International Journal of Hydrogen Energy*, 2022, **47**, 25471-25878, DOI: 10.1016/j.ijhydene.2022.06.013.
- 30 J. Liu, J. Xu, S. Sleiman, X. Chen, S. Zhu, H. Cheng and J. Huot, *International Journal of Hydrogen Energy*, 2021, **46**, 28709-28718, DOI: 10.1016/j.ijhydene.2021.06.137.
- 31 H. Zhao, P. Yao, Y. Zhao, Z. Zeng, C. Xia and T. Yang, *Alloys and Compounds*, 2023, DOI: 10.1016/j.jallcom.2023.170665.
- 32 H-L. Chen, H. Mao and Q. Chen, *Materials Chemistry and Physics*, 2018, **210**, 279- 286, DOI: 10.1016/j.matchemphys.2017.07.082.
- 33 G. Zepon, D.R. Leiva, R.B. Strozi, A. Bedoch, S.J.A. Figueroa, T.T. Ishikawa and W.J. Botta, *International Journal of Hydrogen Energy*, 2018, **43**, 1702-1708, DOI: 10.1016/j.ijhydene.2017.11.106.
- 34 J. Chen, H. Huang, T. Xu, Y. Lv, B. Liu, B. Zhang, J. Yuan and Y. Wu, *International Journal of Hydrogen Energy*, 2024, **50**, 1223-1233, DOI: 10.1016/j.ijhydene.2023.09.121.
- 35 A. Martinez-Garcia, I. Estrada-Guel, E. Reguera, R. Amaro-Hernandez, S. González, C.G. Garay-Reyes and R. Martínez-Sánchez, *International Journal of Hydrogen Energy*, 2024, **50**, 670-684, DOI: 10.1016/j.ijhydene.2023.07.341.
- 36 Z. Wang, Y. Huang, Y. Yang, J. Wang and C.T. Liu, *Scripta Materialia*, 2015, **94**, 28-31, DOI: 10.1016/j.scriptamat.2014.09.010.
- 37 M.G. Poletti and L. Battezzati, *Acta Materialia*, 2014, **75**, 297-306, DOI: 10.1016/j.actamat.2014.04.033.
- 38 I. Toda-Caraballo and P.E.J. Rivera-Díaz-del-Castillo, *Intermetallics*, 2016, **71**, 76-87, DOI: 10.1016/j.intermet.2015.12.011.
- 39 D.J.M. King, S.C. Middleburgh, A.G. McGregor and M.B. Cortie, *Acta Materialia*, 2016, **104**, 172-179, DOI: 10.1016/j.actamat.2015.11.040.
- 40 J. Ma and C. Huang, *Journal of Energy Storage*, 2023, **66**, 107419, DOI: 10.1016/j.est.2023.107419.

- 41 G. Zepon, B.H. Silva, C. Zlotea, W.J. Botta and Y. Champion, *Acta Materialia*, 2021, DOI: 10.1016/j.actamat.2021.117070.
- 42 J.B. Ponsoni, V. Aranda, T.S. Nascimento, R.B. Strozzi, W.J. Botta and G. Zepon, *Acta Materialia*, 2022, DOI: 10.1016/j.actamat.2022.118317.
- 43 A. Mohammadi, Y. Ikeda, P. Edalati, M. Mito, B. Grabowski, H-W. Li and K. Edalati, *Acta Materialia*, 2022, DOI: 10.1016/j.actamat.2022.118117.
- 44 K. Edalati, R. Floriano, P. Edalati, A. Mohammadi, Y. Li, G. Zepon and H-W. Li, *Scripta Materialia*, 2019, 387-390, DOI: 10.1016/j.scriptamat.2019.12.009.
- 45 G. Andrade, B.H. Silva, G. Zepon and R. Floriano, *International Journal of Hydrogen Energy*, 2024, **51**, 246-254, DOI: 10.1016/j.ijhydene.2023.11.111.
- 46 G. Andrade, G. Zepon, K. Edalati, A. Mohammadi, Z. Ma, H-W. Li and R. Floriano, *International Journal of Hydrogen Energy*, 2023, DOI: 10.1016/j.ijhydene.2022.12.134.
- 47 R. Floriano, G. Zepon, K. Edalati, G.L.B. Fontana, A. Mohammadi, Z. Ma, H-W. Li and R.J. Contieri, *International journal of Hydrogen Energy*, 2021, DOI: 10.1016/j.ijhydene.2021.04.181.
- 48 R. Floriano, G. Zepon, K. Edalati, G.L.B. Fontana, A. Mohammadi, Z. Ma, H-W. Li and R.J. Contieri. *International journal of hydrogen energy*, 2020, DOI: 10.1016/j.ijhydene.2020.09.047.
- 49 L. Luo, L. Chen, L. Li, S. Liu, Y. Li, C. Li, L. Li, J. Cui and Y. Li, *International Journal of Hydrogen Energy*, 2024, **50**, 406-430, DOI: 10.1016/j.ijhydene.2023.07.146.
- 50 B.H. Toby, *Powder Diffraction*, 2006, **21**, 67-70, DOI: 10.1154/1.2179804.
- 51 Y. Zhu, X-S. Yang, Z-L. Xu, G. C-P. Tsui, Q. Zhou, R. Tang, F. Xiao and K. Chan, *Journal of Energy Storage*, 2024, **75**, 109553, DOI: 10.1016/j.est.2023.109553.
- 52 J. Liang, G. Li, X. Ding, Y. Li, Z. Wen, T. Zhang and Y. Qu, *Journal of Energy Storage*, 2023, **73**, 108852, DOI: 10.1016/j.est.2023.108852.
- 53 H. Zhao, P. Yao, Y. Zhao, Z. Zeng, C. Xia and T. Yang, *Journal of Alloys and Compounds*, 2023, **960**, 170665, DOI: 10.1016/j.jallcom.2023.170665.
- 54 M. Komeili, H. Arabi and F. Pourarian, *Journal of Alloys and Compounds*, 2023, **967**, 171672, DOI: 10.1016/j.jallcom.2023.171672.
- 55 J. Garcés, *Applied Physics Letters*, 2010, 67–70, DOI:10.1063/1.3400221.
- 56 E. Akiba, *Energy Carriers and Conversion Systems*, vol. II.
- 57 S. Dangwal and K. Edalati, *Scripta Materialia*, 2024, **238**, 115774, DOI: 10.1016/j.scriptamat.2023.115774.
- 58 S. Dangwal and K. Edalati, *International Journal of Hydrogen Energy*, 2024, **50**, 626-636, DOI: 10.1016/j.ijhydene.2023.07.327.
- 59 V. Aranda, D.R. Leiva, J. Huot, W.J. Botta and G. Zepon, *Intermetallics*, 2023, **162**, 108020, DOI: 10.1016/j.intermet.2023.108020.
- 60 Y. He, Y. Su, H. Yu and C. Chen, *International Journal of Hydrogen Energy*, 2021, **46**, 7589-7600, DOI: 10.1016/j.ijhydene.2020.11.238.

61 Z.X.Ma, X.L.Xiong, L.N.Zhang, Z.H.Zhang, Y.Yan and Y.J.Su, *Electrochemistry Communications*, 2018, **92**, 24-28, DOI: 10.1016/j.elecom.2018.05.012.

## RESPONSE TO REVIEWS

*Dear Editor,*

*We very much appreciate the reviewer's comments. The letter below presents which are the changes and responses to the referee's report regarding the manuscript "Design of a Ti-Zr-Fe-Ni medium entropy alloy for hydrogen storage at room temperature by thermodynamic calculations and semi-empirical descriptors" (Journal of Energy Storage, EST-D-24-03118) by G. Andrade and R. Floriano et al.*

*The changes are highlighted in yellow in the manuscript. The responses to the reviewer's comments are also given below in blue.*

*With my best regards,*

*G. Andrade and R. Floriano (corresponding author)*

**Reviewer #1:** Ponsoni proposed some empirical parameters in conjunction with thermodynamic calculation tools, for example  $5.8 \leq \text{VEC} \leq 7.0$  and  $1.123 \leq r_A/r_B \leq 1.223$ .  $\delta > 5.0\%$  for the Laves phase formation. You proposed  $\text{VEC} = 6.2-6.5$ ,  $\delta \geq 9.7\%$ , and  $r_A/r_B = 1.149-1.219$  for material screening. what's your basis for determining this criterion? This is not seen in the article. How has your work improved or innovated compared to Ponsoni's 'Design of multicomponent alloys with C14 laves phase structure for hydrogen storage assisted by computational thermodynamic'? I don't see anything new except imitation. Abbreviations should be used in their entirety the first time they appear. Why do nanocrystals form? Water-cooled copper crucible is not the main reason. Explain the reason in depth. There is little point in screening only one alloy for validation and research! Comparison alloys should be added. Figure 7, the alloy completely releases hydrogen in air in a very short time? Why is there a large difference in platform pressure during cycling? The overall organization of the article and the Figures should be carefully designed.

*We appreciate the comments. To initiate our response, it is very important to say that the model utilized to select the alloy does not imitate Ponsoni's method. In that work, the authors utilized a computational thermodynamic-based model to predict the PCI curves of the alloys, i.e., the equilibrium pressure based on the enthalpy and entropy of the plateau. Ponsoni and others indeed calculated the VEC,  $\delta$ , and  $r_A/r_B$  for the selected alloys. However, they selected the alloys using the CALPHAD method. In a completely different approach, we selected the alloys with the aid of a semi-empirical approach applying the parameters in a certain sequence. Furthermore, the values applied in this paper are completely different from the values calculated by Ponsoni. The semi-empirical approach used to select the present alloy was developed independently of Ponsoni's approach. It is important to note that prior studies conducted within our research group (References: 45-48) have laid the foundational groundwork for the approach employed in this study. Notably, our studies were published prior to Ponsoni's work*

*Anyway, the method utilized is not an imitation and provides a reliable method to select C14-based HEAs. The nanocrystals were indeed observed. The main reason for that is still under evaluation. One explanation remains on the small solidification interval of the alloy. In other words, the C14 phase nucleates with a small amount of free energy, right before the end of the liquidus line. In this case, the undercooling provides a high rate of nucleation, preventing the grains from growing. However, we can't assure that the undercooling of the crucible isn't high enough to favor the high rate of nucleation. That depends on a lot of variables, such as the size of the sample and the flow/temperature of the water. In any case, a better explanation was added to the text. We could name several numbers of articles with just one or two alloys as the object of the work. Comparisons between works should be carefully done since the experimental procedures are very sensible to impact the results/performance in the HEAs field. Nevertheless, appropriate*

*comparisons were made in this paper (references n° 47, 48 and 53). We included a better comparison between our results with these references in the “Discussion” section. For C14 alloys with high-pressure equilibrium in hydrogenation, we observe desorption under atmospheric pressure regularly. The range of the PCIs is very similar. That means the plateau pressure (measured at the midpoint of the curves) is very close to each other. However, there is a change in the position of the curves along the ‘x’ axis. This is because of the drop in the capacity along the PCI cycles. We also included this explanation in the manuscript.*

**Reviewer #2:** This paper reports on design of a Ti-Zr-Fe-Ni médium entropy alloy for hydrogen storage at room temperature by thermodynamic calculations and semi-empirical descriptors. This work provided new methods for composition design of hydrogen storage alloys. However, more specific design details and result analysis should be provided. In total, the manuscript should be modified according to the comments below.

1. In the alloy composition design section, it is not clear why Ti, Zr, Fe and Ni were chosen as the main element of MEA and why the restrictions ( $VEC = 6.2-6.5$ ,  $\delta \geq 9.7\%$ , and  $r_A/r_B = 1.149-1.219$ ) were set within the corresponding range. At the same time, it is recommended to describe in more detail how to check the stability of phases during the thermodynamic equilibrium and to confirm the high trend to the formation of the C14 Laves phase.
2. Authors should describe the microstructural characteristics of the alloys in more detail, including the results of image analysis and the relationship between these results and the hydrogen storage properties of the alloy.
3. What are the roles of BCC and C14 phases in the hydrogen storage process of the alloy. Please explain the mechanism in the process of hydrogen storage of the alloy.
4. Experiments on hydrogen release kinetics need to be supplemented, which are important for the study of hydrogen storage alloys.

- 1. We greatly appreciate the comments provided. The stability of the C14 phase was demonstrated in Fig. 1 with the thermodynamic calculation of the equilibrium of phases using Thermocalc. From that, we can see the high tendency to form the C14 phase. That said, this result shows the accuracy of the employed semi-empirical model for the selection of the alloy. Also, in Fig. 2 it is clear that the alloy indeed crystallizes in C14. We added a section in the discussions to clarify this matter.*
- 2. We report this feature in the second and third paragraphs of the discussion section. The microstructural characteristics were carefully analyzed and put in the context of the hydrogen storage properties. Fig. 3 shows the elemental distribution in the BCC secondary phase. That phase is poor in Fe, meaning that the C14 phase has a high amount of Fe. Hence, Fe helps to stabilize the C14 phase because of the elevated contribution to increasing the absolute mixing enthalpy. The hydrogen storage properties of the alloy, such as the reversibility and fast kinetics, have a close relation to its high tendency to form C14 phase. However, the complete explanation lies in the TEM images in which we describe coherent interphase grain boundaries. It was explained that the “presence of nanoscale grains in large quantities means more grain boundaries than expected for large grains, acting as a pathway for hydrogen transport from the surface to the bulk. Even though low-angle coherent grain boundaries are less favorable to nucleate the hydride phase than high-angle grain boundaries, some studies demonstrated that coherent grain boundaries are more favorable to promote the diffusion of hydrogen atoms to the bulk, because of their highly symmetrical interstitial positions”. Therefore, we described in a detailed way the*

*microstructure of the alloy and its implications for the hydrogen storage properties.*

- 3. The alloy is a multiphasic system where the C14 phase is the majority of the structure. The hydrogen absorption and desorption properties of the alloy are mostly driven by the high weight percentage of such phase. The main characteristics of the C14 are good capacity, fast kinetics, and good reversibility, as shown in Fig. 5 and Fig. 6. Since the amount of  $H_2$  absorbed by the alloy is lower than the maximum theoretical capacity of the C14 phase, there is no hydrogenation for the BCC phase. However, we assume there must be a role for the BCC. We believe there is a synergic interaction between the two phases because of the coherent interphase boundary between them, which could have a role in the absorption kinetics. Some of the related references cited in this manuscript also contribute to this discussion (please, see the References 58 and 59, properly cited in this manuscript);*
- 4. In this paper, it was presented 4 PCIs of desorption. The desorption properties were well demonstrated. The alloy releases almost all of the hydrogen. This fact can be checked by the XRD pattern after desorption (please, see Fig. 7). The lattice parameters of the desorbed state are very close to the as-cast.*

**Reviewer #3:** 1. why only one alloy composition was studied? Is it not necessary to change the alloy composition in order to fully verify the conclusion? 2. What is the purpose of studying this medium entropy alloy, and what are the requirements to be met for its hydrogen storage pressure, capacity, etc., which should be explained in the article. 3. what is the reason for the large slope of the hydrogen absorption and discharge plateau of this alloy and how can it be improved? 4. what

is the effect of the biphasic structure of this alloy on the hydrogen storage properties, especially the thermodynamic properties.

- 1. We appreciate the comments. It is important to observe a large number of articles that describe one or two alloys. For example, we can cite ref. 45-48 just in our research group. The main objective of the work is the design of a MEA alloy with the aid of semi-empirical descriptors and thermodynamic calculations. The idea is to select a composition, measure its hydrogen storage properties, and correlate it to the model's effectiveness. If the main objective of the paper were to understand the effect of the composition, it would be necessary to evaluate the effect of the substitution of a given element in the system's properties.*
- 2. Most of the papers explore the hydrogen storage properties of HEAs. There are a few works about MEAs for hydrogen storage. Despite the number of elemental components, the thermodynamics rules the phase equilibrium. We want to show that a medium entropy alloy can form a major C14 phase in equilibrium. Not only that but to compare its hydrogen storage properties with regular C14-based HEAs.*
- 3. The large slope means there is no transition between an infinite hydrogen solid solution in the metallic unit cell spaces and a hydride phase. There is just one mode in which hydrogen diffuses, i.e., the hydride phase nucleates directly from the C14 and BCC. Furthermore, the slope is proportional to the driving force to push the hydrogen atoms through the bulk. The equilibrium pressure taken from the midpoint of the PCI is a function of the equilibrium enthalpy and the entropy of the solution. The equilibrium pressure can be changed by adding or removing an element with high hydrogen formation enthalpy.*

4. *The alloy is a multiphasic system where the C14 phase is the majority of the structure. The hydrogen absorption and desorption properties of the alloy are mostly driven by the high weight percentage of such phase. We assume that there must be a role for the BCC. We believe that there is a synergic interaction between the two phases because of the coherent interphase boundary between them, which could have a role in the absorption kinetics. From the thermodynamic point of view, the hydrogen will interact in different ways regarding each phase because of the difference in the interstitial spaces available for hydrogen in each of them. It is possible to correlate this to the difference in the bond energy between metallic atoms and hydrogen in each of the phases.*

**Reviewer #4:** This study reported the hydrogen storage properties of an original Ti<sub>21</sub>Zr<sub>21</sub>Fe<sub>41</sub>Ni<sub>17</sub> medium-entropy alloy (MEA), designed by theoretical thermodynamic calculations and semi-empirical descriptors (valence electron concentration, atomic size mismatch, and atomic radius ratio of hydride-forming to non-hydride forming element) was investigated. The applied empirical descriptors and thermodynamic computational calculations to select the C14-based alloy in this study can be principally used to design other MEAs from other systems for hydrogen storage. However, I still have some questions and suggestions about this manuscript. 1. The as-cast alloy is activated by holding at 450°C for 3 hours and then rapidly cooling to room temperature. What are the specific conditions for rapid cooling? And the article mentioned that this process would not produce phase transformation. Could you provide experimental evidence? 2. The SEM picture in Figure 3 is not labeled. It is suggested to label "(a)". 3. The article does not clearly explain which elements are enriched in BCC and C14 phases respectively. It is suggested to add charts or texts to describe them, and use arrows to mark the gray regions and dark regions in the SEM picture in Figure 3 to indicate which is BCC phase or C14 phase. 4. It is suggested to expand the scanning regions range of EDS in Figure 3. Only scanning a dark regions may lead to data errors. 5. It is suggested to adjust the placement of the

pictures in Figure 4. The placement in the article is not conducive to the reader's viewing. 6. The second hydrogen absorption curve in Figure 5 appeared obvious left shift, and the XRD results in Figure 7 do not conform to the description in the article, and the BCC phase appeared obvious left shift after dehydrogenation. Combined with the left shift of the hydrogen absorption curve in Figure 5, one possible reason is that the first dehydrogenation of the BCC phase is not complete. It is suggested to retest the PCT curve and XRD results, and modify the corresponding cycle test results in Figure 6. 7. The cycle test shown in Figure 6 is only conducted for 10 times, which I think is far from enough. Compared with the ninth hydrogen absorption process, the tenth hydrogen absorption process again appeared the phenomenon of reduced hydrogen absorption, and there is no subsequent cycle data for comparison. The curve did not tend to be stable, and the data is not rigorous. I suggest continuing to expand the number of cycles, and explain the reasons for the decrease in hydrogen absorption through experiments or references. 8. The enthalpy of mixing value between Zr-Fe mentioned in the article is -118.4 KJ/mol. Because the negative value of the enthalpy of mixing is very large, the Fe element plays a role in stabilizing the C14 phase. I suggest the author provide the calculation method or reference of the enthalpy of mixing, and calculate the mixing enthalpy of Zr-Ti, Zr-Ni, Fe-Ti, Fe-Ni and Ti-Ni, to prove that Zr-Fe does have the largest negative enthalpy in this alloy system, and plays a key role in the stability of C14 phase.

- 1. We appreciate the suggestions. The samples were not rapidly cooled down to room temperature. We mentioned "immediately colling down to room temperature", however, this statement does not reflect the actual experimental procedure. The alloy was left to cool down to room temperature by itself. Once the heat source was plugged off, the alloy cooled down to room temperature for several minutes. Thus, the text was changed to a more precise statement. Due to the slow cooling, the alloy does not have any phase transformation. This can be attested by looking at the XRD patterns in the as-cast and after activation/hydrogenation. The alloy is still C14, but the cell parameters changed.*

2. *Done as suggested.*
3. *Done as suggested.*
4. *The dark regions corresponding to the BCC phase have the same contrast in BSE mode along all the areas of Fig. 3-a. Fig. 3-b and the corresponding EDS and elemental mapping focused on one of these dark regions. The selected dark region is representative of the microstructure seen in Fig. 3-a. From that, we can ensure the results are correct.*
5. *Done as suggested.*
6. *The translation of the PCI curves to the left means that the absorption capacity is decreasing along the cycles, which is in agreement with the kinetics results of Fig. 6. It was shown that the cell parameters after the desorption are very close to the as-cast. That means the alloy releases almost all hydrogen. We do not expect a relation between the left displacement of the PCI curves and the correspondent change in the XRD pattern, because the diffraction was done after the complete desorption of the alloy. Despite the main BCC peak being translated to the left in Fig. 7, there is no hydrogen absorption for the BCC. This is because the theoretical hydrogen absorption capacity of the C14 phase is  $H/M = 1$ , which means a maximum capacity of approximately 1.607 wt.% of hydrogen for the alloy. Since the alloy absorbed less than the maximum capacity, the BCC phase does not absorb hydrogen and there is no dehydrogenation for the BCC.*
7. *The drop in the capacity of the 10<sup>th</sup> cycle is irrelevant compared to the drop of the 2<sup>nd</sup> cycle. Hence, there is a tendency for stabilization after the 2<sup>nd</sup> cycle. Anyway, the maximum capacity is not the main parameter for kinetics, since the most important is the behavior of the curve over time.*

8. *The interaction parameter Zr-Fe is an empirical value, as well as for Zr-Ti, Zr-Ni, Fe-Ti, Fe-Ni and Ti-Ni. It does not come from calculations but is a parameter to calculate the mixing enthalpy of the alloy. The additional data was added as suggested.*

**Design of a Ti-Zr-Fe-Ni medium entropy alloy for hydrogen storage at room temperature  
by thermodynamic calculations and semi-empirical descriptors**

Gaspar Andrade<sup>1</sup>, Payam Edalati<sup>1</sup>, Shivam Dangwal<sup>2</sup>, Kaveh Edalati<sup>2</sup>, Ricardo Floriano\*<sup>3</sup>

<sup>1</sup>Postgraduate Program in Mechanical Engineering, School of Mechanical Engineering,  
University of Campinas (FEM-UNICAMP), 200 Mendeleev St., Barão Geraldo, 13083-860,  
Campinas, São Paulo, Brazil

<sup>2</sup>WPI, International Institute for Carbon-Neutral Energy Research (WPI-I2CNER), Kyushu  
University, Fukuoka 819-0395, Japan

<sup>3</sup>School of Applied Sciences, University of Campinas (FCA-UNICAMP), Pedro Zaccaria, 1300,  
13484-350, Limeira, Brazil

**Corresponding author:** Ricardo Floriano

[rflorian@unicamp.br](mailto:rflorian@unicamp.br)

## ABSTRACT

This study employs the mechanisms that rule the hydrogen storage properties, especially the influence of compositional and microstructural factors on thermodynamics and kinetics, to design a medium-entropy alloy derived from the Ti-Zr-Fe-Ni system. A novel non-equiatomic alloy ( $\text{Ti}_{21}\text{Zr}_{21}\text{Fe}_{41}\text{Ni}_{17}$ ) was designed by applying semi-empirical models and computational thermodynamic calculations using the CALPHAD method. Four criteria were followed for design: valence electron concentration  $\text{VEC} = 6.2\text{-}6.5$ , atomic size mismatch  $\delta \geq 9.7\%$ , atomic radius ratio of hydride-forming to non-hydride forming element  $r_A/r_B = 1.149\text{-}1.219$ , and the C14 Laves structure stability as the major phase. The designated material was synthesized by casting and structural analysis showed that the alloy crystallizes as a major C14 phase (92.8 wt%) and a minor BCC phase. Transmission electron microscopy showed the presence of nanograins with a strong tendency to form coherent boundaries between the C14 grains and the interphase of C14 and BCC grains. The alloy showed very fast kinetics after a simple thermal activation and reversibly absorbed 1.4 wt% of hydrogen with a relatively small hysteresis between the cycles. For the kinetics properties, it was suggested that the hydride phase nucleates preferably in coherent grain boundaries resulting in the fast hydrogenation of the alloy. For thermodynamic properties, chemical composition designed by the four mentioned criteria should be considered, while iron also plays a critical role. The high atomic percentage of iron (41%) – a non-hydride forming element – stabilizes the C14 phase because of the elevated absolute contribution of the interaction parameter ( $\Omega_{ij}$ ) of the pair Fe-Zr, ( $\Omega_{ij} = -118.4$  kJ/mol), which results in a negative enthalpy of the mixture, with the C14 structure.

**Keywords:** Metal hydrides; Medium-entropy hydrides; Solid-state hydrogen storage;

## Introduction

High Entropy Alloys (HEAs) are known as a new class of materials with remarkable structural and functional properties<sup>1-4</sup>. Several attempts to propose a definition of HEAs have been made<sup>5</sup>. It is accepted that HEAs are composed of at least five principal elements mixed to produce a single-phase solid solution<sup>6</sup>. The mixing entropy ( $\Delta S_{\text{mix}}$ ) is the thermodynamic quantity generally used to classify the multi-principal element alloys. In this sense, HEAs usually fit in the interval where  $\Delta S_{\text{mix}} > 1.5R$  ( $R$ : universal gas constant). Medium-entropy alloys (MEAs) are classified when  $R < \Delta S_{\text{mix}} < 1.5R$ . Finally, the low-entropy alloys (LEAs) are considered when  $\Delta S_{\text{mix}} \leq R$ <sup>7</sup>. HEAs and MEAs are sometimes classified as multicomponent alloys<sup>8</sup>.

Since the beginning of the last decade, HEAs have been explored as potential materials for solid-state hydrogen storage<sup>9-12</sup>. Most of the hydrogen storage materials based on HEAs investigated so far fall within the category of solid solution alloys, incorporating elements with strong attraction to hydrogen, such as Ti, Zr, Nb, Hf, Ta, and V<sup>13-15</sup>. These alloys create highly stable hydrides that require inconveniently high temperatures, exceeding 400 °C, for the release of hydrogen. This characteristic restricts the practical application of these HEAs and their hydrides<sup>16-19</sup>.

In the field of hydrogen storage, a key challenge lies in discovering a material or hydride that can meet several criteria simultaneously. These include essential factors such as the ability to efficiently absorb and release hydrogen at room temperature in a reversible way, fast kinetics, easy activation, long-term cycling stability, suitable storage at a pressure close to atmospheric level, and high gravimetric capacity<sup>20-28</sup>. Given the significant impact of alloy composition on these hydrogen storage properties, HEAs offer an expansive compositional space to explore, presenting boundless opportunities to tailor these properties<sup>29-31</sup>.

The extensive compositional features of HEAs have been partly investigated using various methods rooted in thermodynamics. These methods encompass semi-empirical rules/descriptors, *ab initio* calculations, and the CALPHAD (Calculation of Phase Diagrams) approach<sup>32</sup>. These methods have a high potential for a deeper fundamental understanding of the phases existing within the HEAs system, their stability, and their correlation with specific desired attributes for hydrogen storage properties<sup>33-35</sup>. For example, valence electron concentration (VEC) has been correlated to hydrogen storage properties, and VEC = 6.4 was suggested to be favorable for low-temperature hydrogen absorption with good capacities and almost full reversibility<sup>36</sup>.

The stability of constituent phases within HEAs stands as a critical matter because of its strong impact on the hydrogen storage properties<sup>37-39</sup>. It was demonstrated that single-phase HEAs can be formed under specific combinations of mixing enthalpies ( $\Delta H_{\text{mix}}$ ), atomic size mismatches ( $\delta$ ), electronegativity mismatches ( $\Delta\chi$ ), and VEC<sup>40</sup>. These parameters vary between solid solution alloys and intermetallic compounds, where a solid solution usually forms for  $\delta \leq 6.6\%$ <sup>36</sup>. Another important parameter is the ratio of atomic radii between A and B components, where A indicates high hydrogen affinity elements and B indicates low hydrogen affinity elements. It was established that when the atomic radius ratio of hydride-forming to non-hydride-forming element  $r_A/r_B > 1.116$ , multicomponent alloys form multiphase or amorphous structures rather than single-phase crystalline structures<sup>41</sup>.

In a recent study by Ponsoni et al.<sup>42</sup>, they explored the influence of VEC,  $r_A/r_B$ , and  $\delta$  assisted by the CALPHAD method on the phase stability of AB<sub>2</sub>-type alloys (A: Ti, Zr, Nb; B=V, Cr, Mn, Fe, Co, Ni, Cu, and Zn) concerning their potential applications as hydrogen storage materials. A total of 1208 compositions (854 equiatomic and 354 non-equiatomic) were evaluated by phase stability. All 354 non-equiatomic alloys and 86 equiatomic compositions were predicted to form the C14

Laves phase. The high incidence of C14 was found for  $5.8 \leq \text{VEC} \leq 7.0$  and  $1.123 \leq r_A/r_B \leq 1.223$ . For  $\delta$ , the values were always higher than 5.0% for the Laves phase formation. Later studies also explored not only AB<sub>2</sub>-type alloys but also other stoichiometries starting from these elements <sup>43</sup>. Despite these studies, the hydrogen storage properties of these alloys and affecting factors for the design remain an open question.

In an attempt to select an intermetallic C14 Laves phase based on HEAs operating at room temperature, the current authors proposed three criteria: (i) AB<sub>2</sub>-type configuration, (ii) C14 Laves single-phase structure, and (iii) VEC of 6.4. Using the previous approach, an AB<sub>2</sub>-type HEA TiZrCrMnFeNi alloy was designed, which exhibited 1.7 wt% hydrogen absorption at room temperature <sup>44</sup>. Later, using first-principles calculations it was shown that the reason for the effectiveness of these criteria lay in the low hydrogen binding energy for room-temperature hydrogen storage <sup>43</sup>, which was also experimentally confirmed in a study about Zr-based HEAs <sup>45</sup>. These criteria were also generalized to other stoichiometries to select C14-based HEA such as TiZrNbFeCrNi <sup>46</sup>, TiZrNbCrFe <sup>47</sup>, and TiZrNbFeNi <sup>48</sup>. These alloys showed a major C14 Laves phase with a small amount of BCC phase. It was confirmed that when VEC is set to values near 6.4, the alloys could reversibly absorb hydrogen with a simple activation process, mostly at room temperature with fast kinetics <sup>43-48</sup>. Although all these studies paid attention to the entropy of mixing due to a large number of principal elements, the enthalpy of mixing is an important parameter in MEAs that was not considered in these studies. It is then necessary to go deeper into the role of  $\Delta H_{\text{mix}}$  on the stabilization of the Laves phases-based MEAs. Moreover, despite some recent progress <sup>49</sup>, the significance of secondary phases in C14-based alloys and their influence on the nucleation of the hydride is still an open issue. An understanding of these issues can facilitate the design of multicomponent alloys for hydrogen storage.

In this study, by considering the influence of compositional and microstructural factors we propose a new design strategy for MEAs for hydrogen storage in a model Ti-Zr-Fe-Ni system. The designed alloy –  $\text{Ti}_{21}\text{Zr}_{21}\text{Fe}_{41}\text{Ni}_{17}$  – was selected by applying both computational thermodynamic calculations using CALPHAD and semi-empirical descriptors to obtain C14 Laves as the major phase. The alloy was produced by arc melting under an argon atmosphere and studied by detailed structural and microstructural characterizations via X-ray diffraction (XRD), scanning electron microscopy (SEM), and transmission electron microscopy (TEM). Hydrogen storage properties at room temperature were also systematically investigated, and the correlations between secondary phase and hydrogen storage properties were discussed.

## **Material and methods**

To select new MEAs for room-temperature hydrogen storage, a semi-empirical and thermodynamics-based method was applied. Firstly, hydride-forming elements A (Zr, Ti, Nb, and V) and non-hydride-forming elements B (Cr, Mn, Fe, Ni, and Co) were selected to combine in some different stoichiometries such as AB, AB<sub>2</sub>, AB<sub>1.5</sub>, and A<sub>1.5</sub>B, resulting in a total of 230 possible compositions. In the second step, some restrictions were applied to obtain compositions with a high tendency to form the C14 Laves phase, in the following order: VEC = 6.2-6.5,  $\delta \geq 9.7\%$ , and  $r_A/r_B = 1.149-1.219$ . The VEC was calculated with the weighted average of the VEC of each element in the alloy, considering their stoichiometry. For the atomic size mismatch ( $\delta$ ), it was taken into account the standard deviation of the atomic radius of the elements of the alloy. Finally, the  $r_A/r_B$  was calculated as the ratio between the average atomic radius of the elements positioned in the A sites and B sites of the C14 unit cell.

The selection resulted in 20 original alloy compositions. These alloys were carefully evaluated by the CALPHAD method using Thermocalc to check the stability of phases during the thermodynamic equilibrium and to confirm the high trend to the formation of the C14 Laves phase. Following these procedures,  $\text{Ti}_{21}\text{Zr}_{21}\text{Fe}_{41}\text{Ni}_{17}$  MEA was chosen as the object of this study, to determine its hydrogen storage properties.

The alloy was experimentally prepared through arc melting of high-purity elemental powders of Zr (99.5%), Ti (99.99%), Fe (99.97%), and Ni (99.99%). The process of arc melting was executed utilizing a non-consumable tungsten electrode and a water-cooled copper crucible under a high-purity argon atmosphere. To enhance chemical uniformity, the ingots underwent six rotations and remelting cycles, while the mass loss was negligible. Subsequently, the ingots were cut into smaller pellets for further microstructural characterization and hydrogen storage measurements.

For crystal structure analysis, the alloy was crushed into micro-sized powders and subjected to XRD measurements. The XRD analysis utilized a Cu-K $\alpha$  radiation source ( $\lambda = 0.15406$  nm) with an X'Pert Panalytical diffractometer operating at 45 kV and 40 mA. The Rietveld refinement method, in conjunction with GSAS-II software, was employed to determine the lattice parameters, phase fractions (wt%), crystallite size, and isotropic microstrain. The refinement process included adjusting background estimation using a Chebyshev background function with five coefficients, determining phase fractions, and refining lattice parameters. The resulting refinements demonstrated residual values (Rwp) and goodness-of-fit (GOF) below 5%, affirming the high quality and reliability of the results<sup>50</sup>.

Microstructural investigations were conducted using SEM and high-resolution TEM. For SEM, the samples underwent mechanical polishing with colloidal silica of 60 nm particle size. The polished samples were examined using a Philips XL-30 FEG SEM equipped with energy-

dispersive X-ray spectroscopy (EDS). Back-scattered electron and secondary electron (BSE and SE) images, along with elemental mapping at different magnifications in selected regions, were captured for all samples. For TEM analysis, ethanol was used as a medium to crush the alloy while preventing oxidation. After being crushed, the sample was dispersed onto a carbon grid and immediately examined by TEM.

To assess hydrogen storage performance, pressure-composition-temperature (PCT) absorption and desorption isotherms, along with kinetic measurements under a hydrogen pressure of 3.5 MPa, were carried out at room temperature by using a Sieverts-type machine. Samples weighing approximately 250 mg were crushed in air followed by passing the crushed powders through a sieve of 75  $\mu\text{m}$  size.

The hydrogenation measurements were first conducted without any activation treatment, but since the alloys did not absorb hydrogen, an activation procedure was applied. The activation procedure applied consisted of increasing the temperature to 450 °C for 3h under a dynamic vacuum and left to cool down to room temperature by itself. It is important to mention that the activation procedure does not lead to any structural phase transitions, due to the small temperature compared to the melting point of the alloys. Selected samples were examined by XRD after hydrogenation, and in this case, the samples were examined by XRD in less than 5 min after their removal from the reactor of the Sieverts machine.

## Results

**Fig. 1** shows the phase diagram of the designed alloy determined by Thermocalc. The thermodynamic computational calculation indicates that the alloy crystallizes with the majority of

the C14 phase in the equilibrium. Furthermore, considering the large solidification interval, the C14 phase remains stable in the liquid phase and grows at elevated temperatures (1800 °C) until its complete solidification. Although the thermodynamic equilibrium foresees other phases such as BCC in temperatures below 750 °C, their fractions are very low, under 10% of all phases.

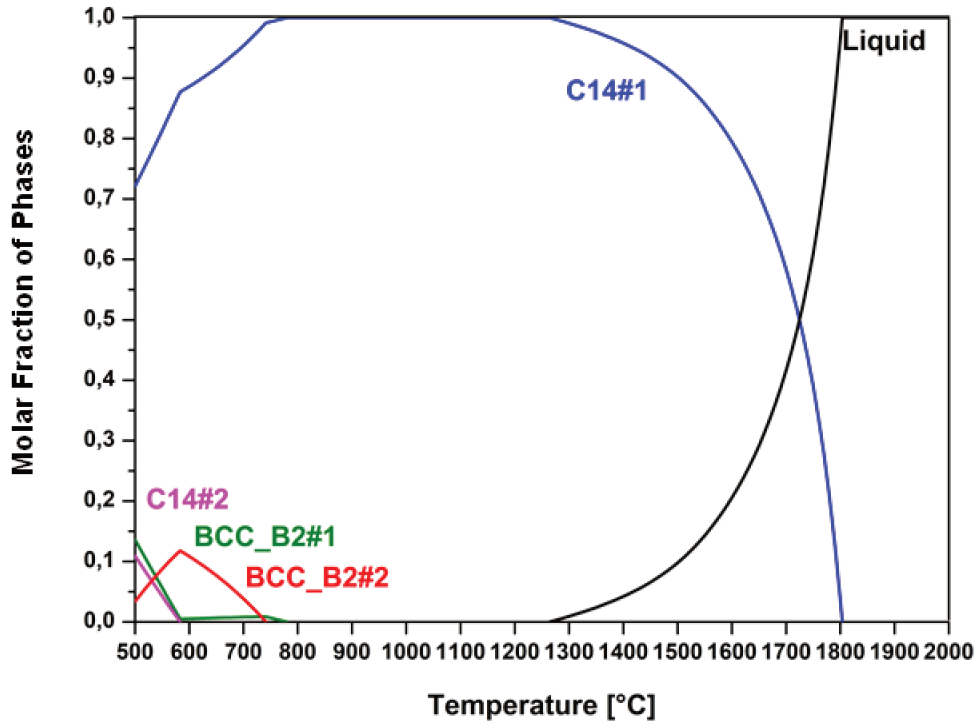


**Figure 1:** Molar fraction of equilibrium phases as a function of temperature calculated for the  $Ti_{21}Zr_{21}Fe_{41}Ni_{17}$  alloy using CALPHAD and TCHEA3 database.

**Table 1** shows the atomic fraction of each element in the C14 phase of the referred composition, determined by CALPHAD. The occupation factor of each element in the C14 unit cell was used later to determine the structural parameters by the Rietveld refinement.

**Table 1 – Structural parameters of the C14 unit cell in  $Ti_{21}Zr_{21}Fe_{41}Ni_{17}$  alloy.**

Phase	Atom	Wyckoff position	Molar fraction	Occupation factor
C14	Zr	4f (1/3, 2/3, 0.06030)	0.21	0.62
	Ti		0.21	0.38
Space Group: P63/mmc (194)	Fe	2a (0, 0, 0)	0.41	0.61
	Ni		0.17	0.26
	Ti		-----	0.13
	Fe	6h (0.83170, 0.66340, 1/4)	-----	0.61
	Ni		-----	0.26
	Ti		-----	0.13

**Fig. 2** and **Fig. 3** show the XRD patterns with the corresponding Rietveld refinement and the SEM/EDS images of the  $Ti_{21}Zr_{21}Fe_{41}Ni_{17}$  alloy, respectively. The Rietveld refinement was done by using the crystal structure data displayed in **Table 1** which was built by using the information of the composition and the constitution of the calculated C14 Laves phase at 1000 °C. The agreement indices for the refinement are GOF = 1.45 and Rwp = 3.022. The structural parameters of the C14 phase, as determined by Rietveld, are  $a = 4.968 \text{ \AA}$  and  $c = 8.079 \text{ \AA}$ . The Rietveld refinement indicates that the alloy crystallizes as a major C14 phase – 92.8 wt% – and a minor BCC phase – 7.2 wt%, in good agreement with the calculated phase diagram in **Fig. 1**. These results agree with the SEM images shown in **Fig. 3-a** and **Fig. 3-b**, where it is evident the existence

of a two-phase microstructure. The elemental mappings shown in **Fig. 3** suggest that some elements tend to occupy one phase instead of another. For example, a higher concentration of Ni and Ti in the dark regions detached in **Fig. 3-b** is observed, while at the same time, these areas are poor in Fe. On the other hand, Zr is very well distributed in the whole microstructure, meaning that this element is present in both C14 and BCC phases. It should be also noted in the EDS spectra taken from the whole area in **Fig. 3-c** that the atomic fraction of each element is very close to the nominal percentage of these elements in the referred alloy.

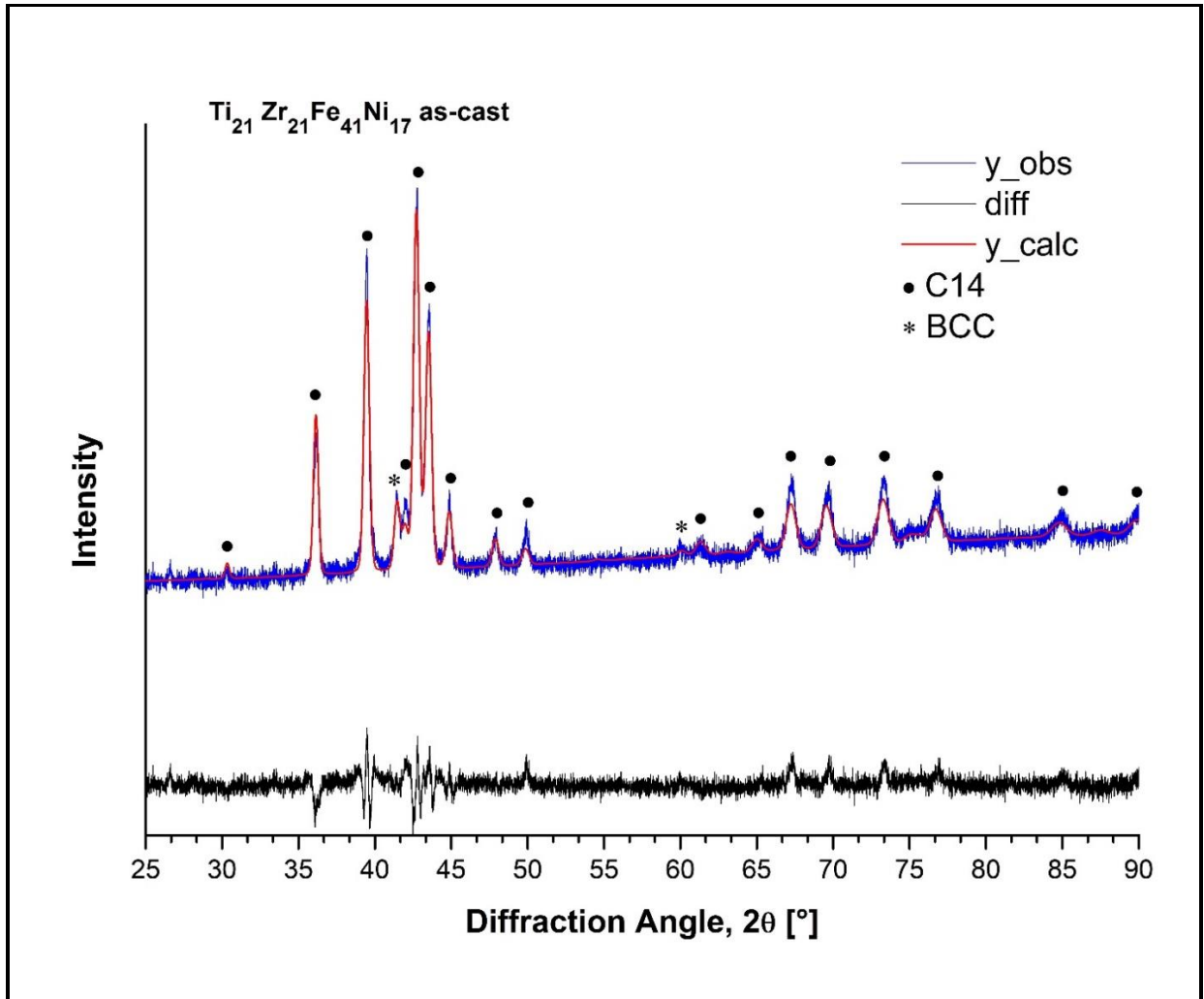


**Figure 2:** XRD pattern and Rietveld refinement of the  $\text{Ti}_{21}\text{Zr}_{21}\text{Fe}_{41}\text{Ni}_{17}$  alloy in the as-cast condition.

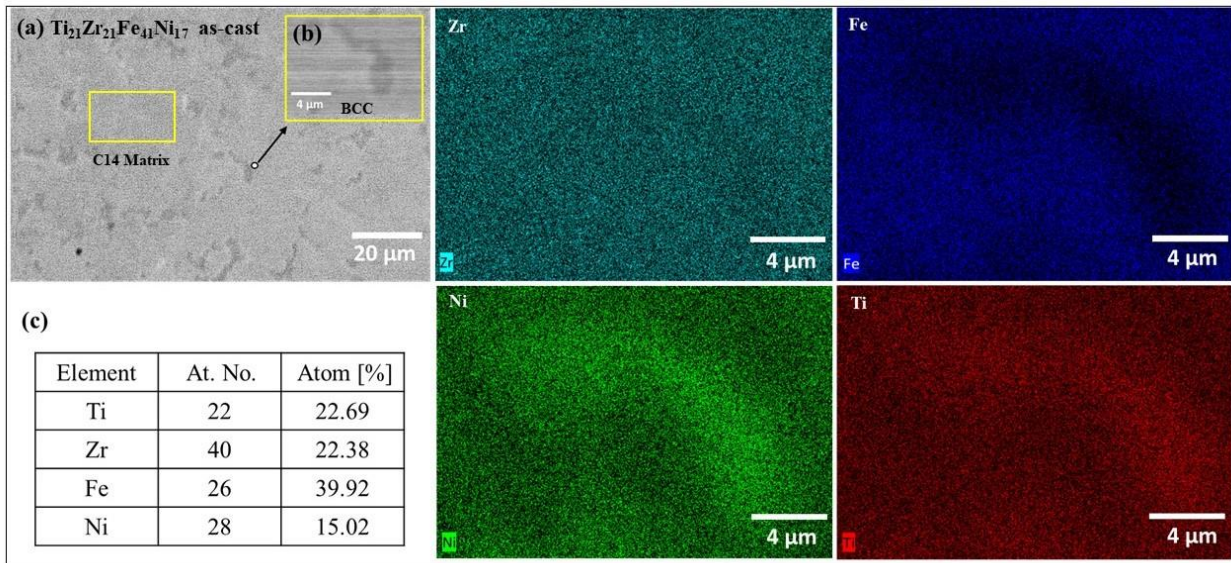


**Figure 3:** SEM images and corresponding EDS elemental mappings of  $Ti_{21}Zr_{21}Fe_{41}Ni_{17}$  alloy in the as-cast condition. **a)** SEM images using BSE mode, **b)** magnified view of BSE image, **c)** EDS maps and quantification of the selected BSE area in (b).

**Fig. 4** shows TEM images: **a)** bright field (BF), **b)** SAED pattern, and **c)** dark field (DF) of the  $Ti_{21}Zr_{21}Fe_{41}Ni_{17}$  alloy in the as-cast state. The DF image was taken from the location of the diffracted rays indicated by the yellow arrow in the SAED pattern. The High-resolution TEM image in **Fig. 4-d** shows some nanograins, where the crystal directions are indexed using the fast Fourier transform (FFT) analysis. As can be seen, both BCC and C14 Laves phases are crystallized next to each other in this type of grain. **Fig. 4-e** and **Fig. 4-f** show the two grain boundaries selected with yellow squares in a higher magnification. **Fig. 4-g** shows one of these larger grains that contains a dislocation. **Fig. 4-h**, prepared using the Inverse FFT technique from the yellow square area, clearly shows the existence of this dislocation.

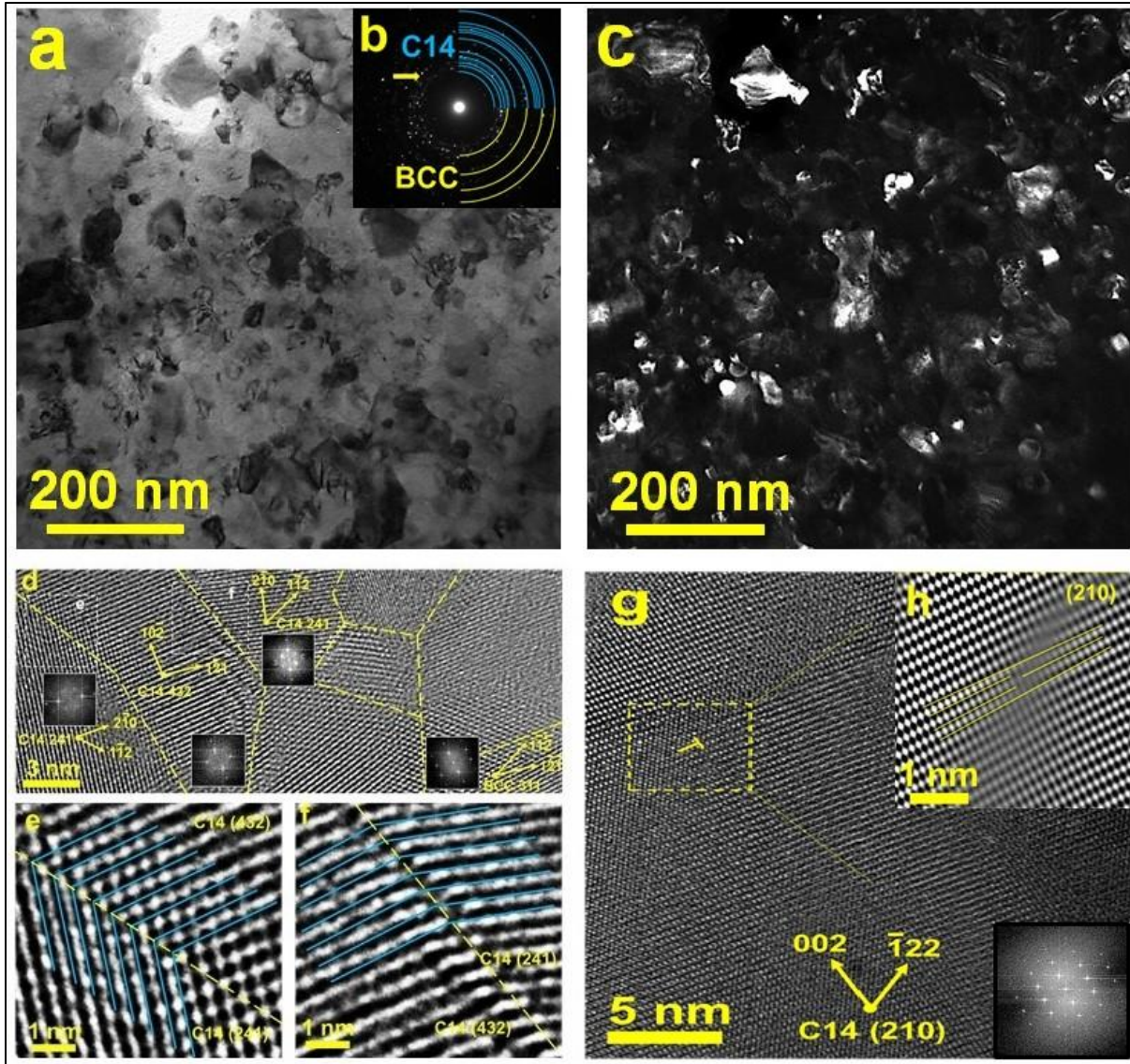


**Figure 4:** TEM images of the  $\text{Ti}_{21}\text{Zr}_{21}\text{Fe}_{41}\text{Ni}_{17}$  alloy in the as-cast state. **a)** BF image, **b)** SAED pattern, **c)** DF image, **d)** high-resolution image showing nanoscale C14 and BCC grains, **e-f)** lattice images showing coherent grain boundaries, **g-h)** high-resolution image and corresponding inverse FFT analysis showing dislocations in large grains.

Regarding the hydrogen absorption properties, the PCT isotherm measurements were conducted for the  $\text{Ti}_{21}\text{Zr}_{21}\text{Fe}_{41}\text{Ni}_{17}$  alloy in the as-cast state at room temperature without any activation

procedure. The sample did not show any absorption ability in this condition, and thus, the activation procedure at 450 °C for 3h under dynamic vacuum was applied. **Fig. 5** shows the 4<sup>th</sup> PCT absorption and desorption isotherms of the  $\text{Ti}_{21}\text{Zr}_{21}\text{Fe}_{41}\text{Ni}_{17}$  alloy at room temperature after the activation procedure. Firstly, by looking at all PCT absorption and desorption isotherms, the absence of a well-defined equilibrium plateau pressure is evident. Secondly, the alloy starts to absorb hydrogen at very low pressure, of the order of kilopascal, in the first absorption. The alloy absorbs 1.4 wt% of hydrogen (subtracted from the initial 0.2 wt%) and showed a very good reversibility at room temperature desorbing almost the same amount of hydrogen in all cycles.

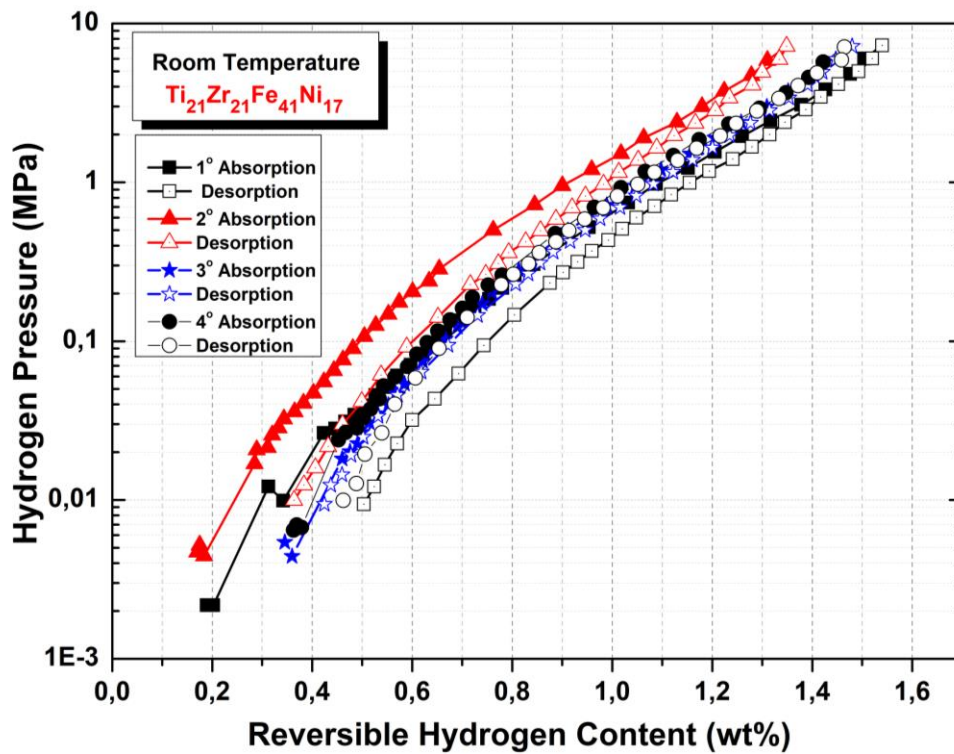


**Figure 5:** PCT absorption/desorption isotherms at room temperature for  $\text{Ti}_{21}\text{Zr}_{21}\text{Fe}_{41}\text{Ni}_{17}$  alloy after activation.

Additionally, it's noteworthy that there's a slight shift in the position of the curves along the 'x' axis observed in the PCT curves. This shift is attributed to the decline in hydrogen capacity throughout the PCI cycles, a trend also observed during the kinetic cycling discussed ahead.

**Fig. 6-a** shows the absorption kinetics of  $\text{Ti}_{21}\text{Zr}_{21}\text{Fe}_{41}\text{Ni}_{17}$  alloy at room temperature under a hydrogen pressure of 3.5 MPa after PCT isotherm measurements. As can be shown, the alloy exhibits a very fast absorption kinetics without any incubation time and achieves the maximum capacity of 1.4 wt% of hydrogen after 60 seconds. The cycling test applied to this alloy, as highlighted in **Fig. 6-b**, reveals that the hydrogen storage capacity is quite stable after ten cycles. The maximum capacity of 1.17 wt% remains stable between the 2<sup>nd</sup> and the 10<sup>th</sup> cycles, while a small drop in the capacity can be noticed between the 1<sup>st</sup> to the 2<sup>nd</sup> cycles.

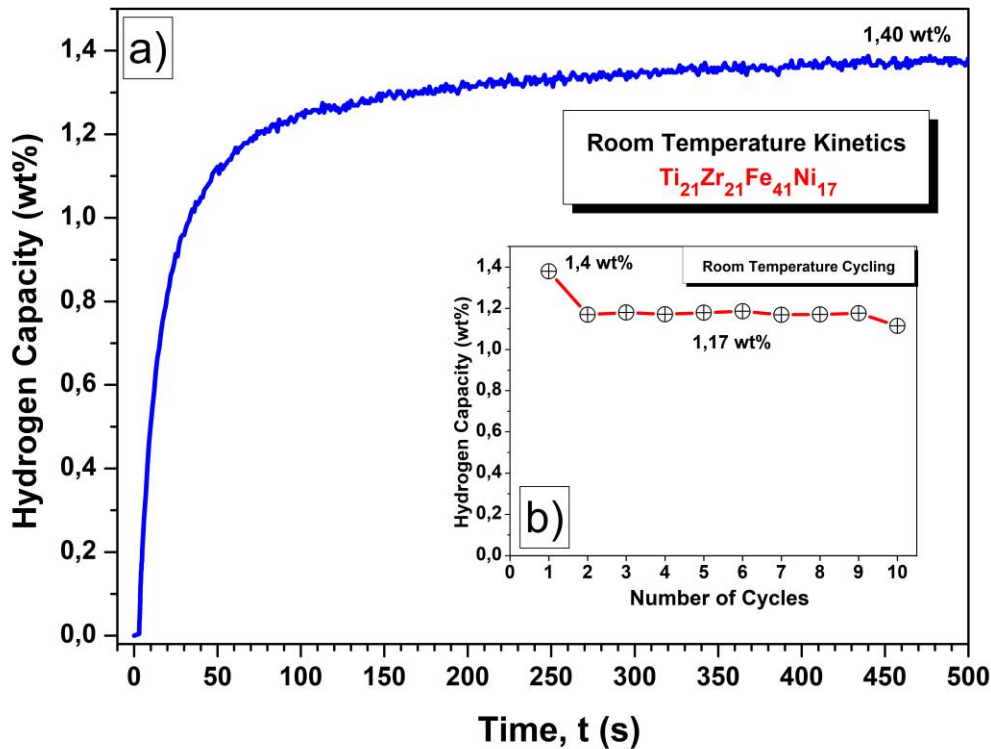


**Figure 6:** a) Kinetic curve of  $\text{Ti}_{21}\text{Zr}_{21}\text{Fe}_{41}\text{Ni}_{17}$  alloy at room temperature under the hydrogen pressure of 3.5 MPa, b) the hydrogen storage capacity as a function of the number of cycles.

The crystal structure of the alloy after hydrogenation was also checked. For comparison, **Fig. 7** shows the XRD patterns and the indexed phases of the alloy in the as-cast state and after hydrogenation. As seen in the image, there is no shift in the angular positions of the C14 peaks after hydrogenation compared to the as-cast sample, which means that the alloy immediately releases hydrogen when exposed to atmospheric pressure, even considering the short time between its removal from the reactor and the XRD analysis. The cell parameters for the C14 after spontaneous desorption are  $a = 4.979 \text{ \AA}$  and  $c = 8.096 \text{ \AA}$ , which are very close to the cell

parameters obtained for the as-cast sample. In addition to the detection of the C14 phase, the presence of the BCC phase is also noticed, in agreement with **Fig. 2**.

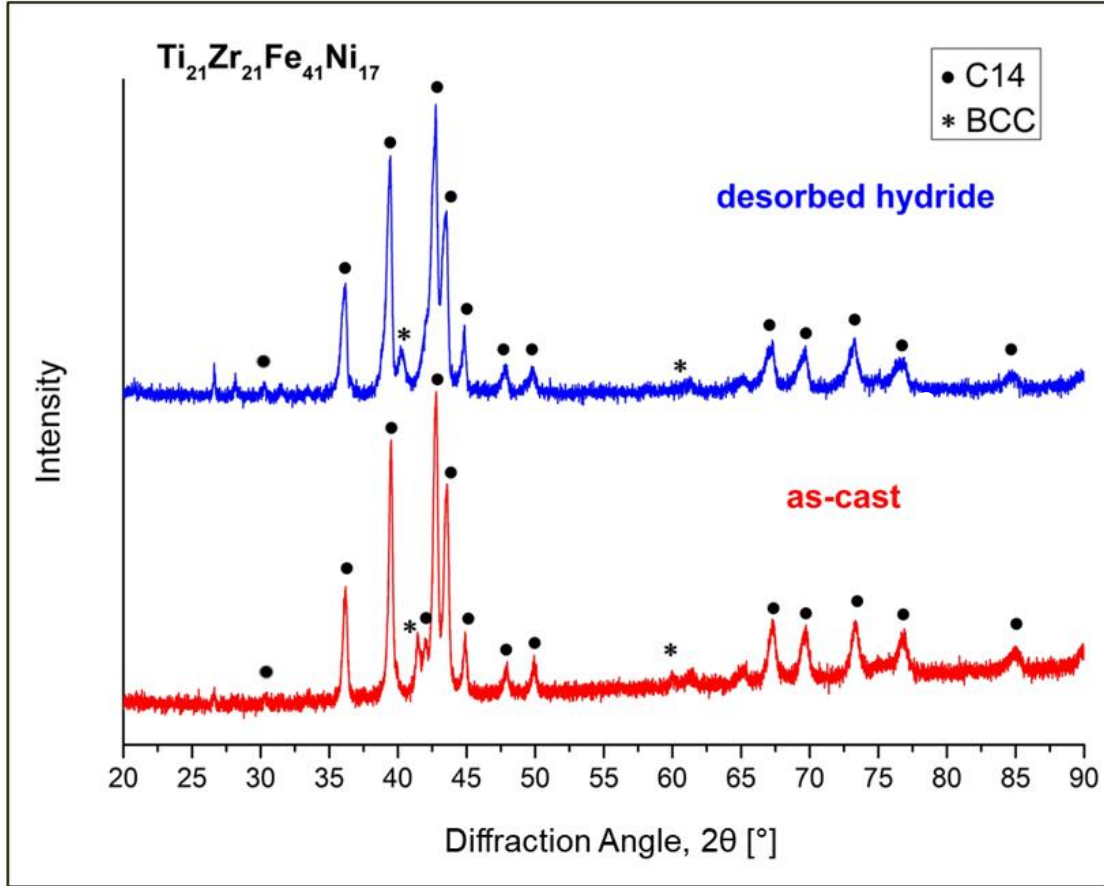


**Figure 7:** XRD patterns of  $Ti_{21}Zr_{21}Fe_{41}Ni_{17}$  alloy in the as-cast and hydrogenated states. Bragg angle positions for C14 and BCC phases were also included as references.

## Discussion

Intermetallic HEAs having the C14 Laves structure as the major phase demonstrated a great ability to absorb and desorb hydrogen at low temperatures<sup>51</sup>, with easy activation<sup>44</sup>. However, studies on MEAs, in which entropy is lower and the enthalpy is more dominant, for hydrogen storage at room temperature are limited. In this study, we applied the combination of semi-empirical descriptors followed by the CALPHAD thermodynamic calculations to design MEAs for hydrogen storage. The results concerning the crystal structure initially predicted using the CALPHAD

method (**Fig. 1**) and subsequently by the XRD (**Fig. 2**), confirmed that the proposed design method correctly selected a  $\text{Ti}_{21}\text{Zr}_{21}\text{Fe}_{41}\text{Ni}_{17}$  alloy with a high tendency to form the majority of the C14 Laves phase stable in the thermodynamic equilibrium. In this section, some structural and microstructural features of the designated alloy and their influence on hydrogen storage properties need to be discussed.

The microstructural analysis represented by the SEM images (**Fig. 3**) showed the appearance of two distinct regions: dark and gray regions. The dark regions refer to the Ti- and Ni-rich regions, which are expected for the composition of the BCC phase according to the CALPHAD prediction. Moreover, the apparent amount of the BCC phase is compatible with the quantity of this phase as determined by the Rietveld refinement. On the other hand, the gray regions that appear in high proportion in the SEM images are associated with the C14 phase. The absence of Fe in the BCC phase and its abundant presence in the C14 Laves phases is noted in EDS analysis. As we will explain later, Fe is responsible for decreasing the enthalpy of the mixture, favoring the crystallization of intermetallic phases, such as the C14 phase.

From the TEM analysis (**Fig. 4**), it can be seen that the grains have crystallized in various sizes ranging from micrometers to nanometers, which is a little abnormal for the sample after casting. One explanation remains on the possible small solidification interval of the alloy. The C14 phase nucleates with a small amount of free energy, right before the end of the liquidus line. In this case, the undercooling provided by the water-cooled crucible during arc melting causes a high rate of nucleation, preventing the grains from growing<sup>52</sup>. The SAED analysis with a ring pattern (**Fig. 4-b**) clearly shows the existence of nanograins of two phases, BCC and C14-Laves, which is consistent with the prediction of thermodynamic simulation with the CALPHAD method and the results of XRD analysis. It is important to pay attention to the grain boundaries of these nanograins

because they show a strong tendency to form coherent grain boundaries with low energy. Unlike large grains, dislocations are not seen in nanograins, which is expected due to the instability of dislocations near grain boundaries.

The PCT cycles of absorption and desorption (**Fig. 5**) show that the alloy can reversibly absorb and desorb a reasonable amount of hydrogen with almost no hysteresis. It is worth pointing out that, the alloy became fully activated after a simple activation procedure as already described in the experimental section. The absence of a well-defined plateau in the PCT curves suggests the hydrogen atoms form a solid solution alongside the metallic atoms. Taking the pressure of 0.1 MPa (1 atm) as a reference line, most parts of the PCT curves are above this level of pressure. This is desirable for hydrogen storage applications because the formed hydride is not so stable, being able to desorb hydrogen at atmospheric pressure. In terms of kinetics (**Fig. 6**), the selected alloy showed a very fast hydrogen absorption after a simple thermal activation step. The maximum amount absorbed of 1.4 wt.% of hydrogen is comparable with other C14-based alloys already reported in the literature. The TiZrNbCrFe<sup>47</sup> alloy was able to absorb 1.35 wt.% at room temperature, while the TiZrNbFeNi<sup>48</sup> absorbed 1.2 wt.% at room temperature, after the same heat treatment activation of 450 °C for 3 hours in a vacuum. Also, the maximum amount of hydrogen remains almost the same after the second cycle. This feature can be attributed to the stability of the C14 phase under hydrogenation/dehydrogenation, since the reaction occurs in a single step, without any intermediate hydride phase<sup>53</sup>.

From the thermodynamic point of view, the reversibility of the alloy can be associated with the calculated value of VEC = 6.5. It was proposed that VEC should be kept around 6.4 to improve the hydrogen storage properties<sup>44,47-48</sup>. Also, the calculated enthalpy of mixture ( $\Delta H_{\text{mix}}$ ) for the Ti<sub>21</sub>Zr<sub>21</sub>Fe<sub>41</sub>Ni<sub>17</sub> alloy is equal to -29 kJ/mol. The Laves phases-based HEAs with  $\Delta H_{\text{mix}}$  of -15 to

-5 kJ/mol are usually considered suitable candidates for hydrogen storage applications as they demonstrate high hydrogen-to-metal (H/M) ratios and favourability for hydride formation enthalpy ( $\Delta H_{\text{form}}$ )<sup>54,55</sup>. A very negative enthalpy of formation such as -29 kJ/mol means that the metallic bonds are strong, and as explained by the Miedema rule, a very stable intermetallic compound (strong metallic bonds) forms an unstable hydride<sup>56</sup>. It should be noted that the strong negative  $\Delta H_{\text{mix}}$  calculated for this alloy with high Fe content (41 at%) comes from the elevated contribution of the interaction parameter ( $\Omega_{ij}$ ) of the pair Fe-Zr, where  $\Omega_{ij} = -118.4$  kJ/mol. The interaction parameters of Zr-Ni (-236.4 kJ/mol) and Ti-Ni (-124.1 kJ/mol) are also significant, but the small atomic percentage of Ni in the alloy tends to decrease its contribution to the final value of the mixing enthalpy. The other contributions are too small, as follows for the Zr-Ti (-0.8 kJ/mol), Fe-Ti (-61.6 kJ/mol), and Fe-Ni (-6.4 kJ/mol). Moreover, since the  $\text{Ti}_{21}\text{Zr}_{21}\text{Fe}_{41}\text{Ni}_{17}$  alloy can be classified as a MEA ( $\Delta S_{\text{mix}} = 8.3$  J/mol. K which is lower than  $1.5R$ , where  $R = 8.31$  J/mol. K), the strong negative  $\Delta H_{\text{mix}}$  plays the main role in stabilizing the intermetallic C14 phase. Taking all together, the high concentration of Fe – a non-hydride forming element – is responsible not just for the good reversibility of the alloy, but also for the stabilization of the C14 phase, which grants good hydrogen absorption properties.

Regarding the mechanisms that could explain the attractive hydrogen storage properties of the  $\text{Ti}_{21}\text{Zr}_{21}\text{Fe}_{41}\text{Ni}_{17}$  alloy, three main reasons are presented here: i) appropriate thermodynamics of the system which was adjusted by semi-empirical descriptors and thermodynamic calculations, ii) the presence of interphase boundaries; and iii) the presence of coherent grain boundaries. In a recent study<sup>57</sup>, it was suggested that the presence of a small amount of a second phase appears to be a good solution to the issue of the activation of some alloys<sup>58</sup>. This is supported by the fact that the interphase boundaries can act like a hydrogen transport medium, which explains the easy

activation of dual-phase alloys<sup>59</sup>. However, it was claimed that the presence of interphase boundaries is not the only mechanism that explains the easy activation in HEAs, because they also can amplify the heterogeneous nucleation of the hydride at grain boundaries. The TEM images showed the presence of nanograins with a strong tendency to form coherent grain boundaries between the C14 grains. A close look at **Fig. 4-d** shows that even some C14/BCC interphase boundaries are coherent. The nucleation of the hydride can be favored due to the reduction of energy of the grain boundaries, which explains the fast kinetics and good reversibility of the alloy. Moreover, the presence of nanoscale grains in large quantities means more grain boundaries than expected for large grains, acting as a pathway for hydrogen transport from the surface to the bulk. Even though low-angle coherent grain boundaries are less favorable to nucleate the hydride phase than high-angle grain boundaries, some studies<sup>60-61</sup> demonstrated that coherent grain boundaries are more favorable to promote the diffusion of hydrogen atoms to the bulk, because of their highly symmetrical interstitial positions.

## Conclusions

This study reported the hydrogen storage properties of an original  $\text{Ti}_{21}\text{Zr}_{21}\text{Fe}_{41}\text{Ni}_{17}$  MEA, designed by theoretical thermodynamic calculations and semi-empirical descriptors (valence electron concentration, atomic size mismatch, and atomic radius ratio of hydride-forming to non-hydride forming element) was investigated. The alloy showed fast kinetics and could reversibly absorb 1.4 wt.% of hydrogen at room temperature with a relatively small hysteresis along the cycles. The structural measurements by the Rietveld refinement show the alloy crystallizes as 92.8% of the C14 phase and a minor amount of the BCC phase, in agreement with the phase diagram obtained by the thermodynamic calculations. Additionally, nanoscale grains were observed with coherent

interphase grain boundaries. It was proposed that the hydride phase nucleates preferably in coherent grain boundaries, which explains the fast kinetics of the alloy. The applied empirical descriptors and thermodynamic computational calculations to select the C14-based alloy in this study can be principally used to design other MEAs from other systems for hydrogen storage.

### Conflicts of interest

There are no conflicts to declare.

### Acknowledgments

This work is supported in part by a grant from the Brazilian Research Funding Agency FAPESP (Regular Project No. 2022/01351-0), and in part by Grants-in-Aid for Scientific Research on Innovative Areas from the MEXT, Japan (JP19H05176 & JP21H00150).

### References

- 1 B. Cantor, I.T.H. Chang, P. Knight and A.J. Vincent, *Materials Science Engineering*, 2004, 357-377, DOI: 10.1016/j.msea.2003.10.257.
- 2 Y. Ye, Q. Wang, J. Lu, C. Liu and Y. Yang, *Materials Today*, 2016, **19**, 349-62. DOI: 10.1016/j.mattod.2015.11.026.
- 3 D.B. Miracle and O.N. Senkov, *Acta Materialia*, 2017, **122**, 448-511, DOI: 10.1016/j.actamat.2016.08.081.
- 4 F. Marques, M. Balcerzak, F. Winkelmann, G. Zepon and M. Felderhoff, *Energy & Environmental Science*, 2021, DOI: 10.1039/d1ee01543e.
- 5 L. Luo, L. Chen, L. Li, S. Liu, Y. Li, C. Li, L. Li, J. Cui and Y. Li, *International Journal of Hydrogen Energy*, 2024, **50**, 406-430, DOI: 10.1016/j.ijhydene.2023.07.146.
- 6 T. R. Somo, M.V. Lototsky, V.A. Yartys, M.W. Davids and S.N. Nyamsi, *Journal of Energy Storage*, 2023, **73**, 108969, DOI: 10.1016/j.est.2023.108969.
- 7 K-F. Yao, H-W. Luan, Y. Shao, J-F. Li, W-L Mao, Z-D. Han and C. Shao, *Scripta Materialia*, 2020, 40-44, DOI: 10.1016/j.scriptamat.2019.12.041.
- 8 S. Akrami, P. Edalati, M. Fuji and K. Edalati, *Materials Science and Engineering*, 2021, **146**, 100644, DOI: 10.1016/j.mser.2021.100644.

- 9 I. Kuncce, M. Polanski and J. Bystrzycki, *International journal of hydrogen energy*, 2013, 12180-12189, DOI: 10.1016/j.ijhydene.2013.05.071.
- 10 Y. Wang, J. Yuan, J. Chen, Z. Li, H. Huang, Y. Lv, B. Liu, Y. Li and Y. Wu, *Scripta Materialia*, 2022, DOI: 10.1016/j.scriptamat.2022.114548.
- 11 S-K. Chen, P-H. Lee, H. Lee, H-T. Su, *Materials Chemistry and Physics*, 2018, 336-347 DOI: 10.1016/j.matchemphys.2017.08.008.
- 12 D.J.M. King, S.C. Middleburgh, A.G. Mcgregor and M.B Cortie, *Acta Materialia*, 2016, **104**, 172-179, DOI: 10.1016/j.actamat.2015.11.040.
- 13 X. Yang and Y. Zhang, *Materials Chemistry and Physics*, 2012, **132**, 233-238, DOI: 10.1016/j.matchemphys.2011.11.021.
- 14 K. Guruvadyathri, M. Vaidya and B.S. Murty, *Scripta Materialia*, 2020, **188**, 37-43, DOI: 10.1016/j.scriptamat.2020.06.060.
- 15 Y.F. Kao, S.K. Chen, J.H. Sheu, J.T. Lin, W.E. Lin, J.W. Yeh, S.J. Len, T.H. Liou and C.W. Wang, *International Journal of Hydrogen Energy*, 2010, **35**, 46-59, DOI: 10.1016/j.ijhydene.2010.06.012.
- 16 M.M. Nygård, G. Ek, D. Karlsson, M.H. Sørby, M. Sahlberg and B.C. Hauback, *Acta Materialia*, 2019, **175**, 121-129, DOI: 10.1016/j.actamat.2019.06.002.
- 17 M.M. Nygård, G. Ek, D. Karlsson, M.H. Sørby, M. Sahlberg and B.C. Hauback, *International Journal of Hydrogen Energy*, 2019, **44**, 29140-29149, DOI: 10.1016/j.ijhydene.2019.03.223.
- 18 M. Sahlberg, D. Karlsson, C. Zlotea and U. Jansson, *Scientific Reports*, 2016, **6**, DOI: 10.1038/srep36770.
- 19 C. Zhang, A. Song, Y. Yuan, Y. Wu, P. Zhang, Z. Lu, X. Song, *International Journal of Hydrogen Energy*, 2020, **45**, 5367-5374, DOI: 10.1016/j.ijhydene.2019.05.214.
- 20 C. Zlotea, M.A. Sow, G. Ek, J.P. Couzinié, L. Perrière, I. Guillot, J. Bourgon, K.T. Møller, T.R. Jensen, E. Akiba and M. Sahlberg, *Journal of Alloys and Compounds*, 2019, **775**, 667-674, DOI: 10.1016/j.jallcom.2018.10.108.
- 21 L. Chanchetti, S.M. Oviedo Diaz, D.H. Milanez, D.R. Leiva, L.I.L. De Faria and T.T. Ishikawa, *International Journal of Hydrogen Energy*, 2016, **41**, 18301-18310, DOI: 10.1016/j.ijhydene.2016.08.137.
- 22 M. Hirscher, V.A. Yartys, M. Baricco, J.B. Von Colbe, D. Blanchard, R.C. Bowman Jr, D.P. Broom, C.E. Buckley, F. Chang, P. Chen, Y.W. Cho, J-C. Crivello, F. Cuevas, W.I.F. David, P.E. De Jongh, R.V. Denys, M. Dornheim, M. Felderhoff, Y. Filinchuk, G.E. Froudakis, D.M. Grant, E.M.A. Gray, B.C Hauback, T. He, T.D. Humphries, T.R. Jensen, S. Kim, Y. Kojima, M. Latroche, H-W. Li, M.V. Lototsky, J.W. Makepeace, K.T. Møller, L. Naheed, P. Ngene, D. Noreus, M.M. Nygård, S. Orimo, M. Paskevicius, L. Pasquini, D.B. Ravnsbæk, M.V. Sofianos, T.J. Udovic, T. Vegge, G.S. Walker, C.J. Webb, C. Weidenthaler and C. Zlotea, *Journal of Alloys and Compounds*, 2020, **827**, DOI: 10.1016/j.jallcom.2019.153548.

- 23 J. Huot, F. Cuevas, S. Deledda, K. Edalati, Y. Filinchuk, T. Grosdidier, B.C. Hauback, M. Heere, T.R. Jensen, M. Latroche and S. Sartori, *Materials*, 2019, **12**, DOI:10.3390/ma12172778.
- 24 R. Cohen, K. West and J. Wernick, *Journal of Less-Common Metals*, 1980, **73**, 273-279. DOI: 10.1016/0022-5088(80)90315-X.
- 25 T. Maeda, T. Fuura, I. Matsumoto, Y. Kawakami and M. Masuda, *Journal of Alloys and Compounds*, 2013, **580**, 255-258, DOI: 10.1016/j.jallcom.2013.03.230.
- 26 X. Zhao, J. Zhou, X. Shen, M. Yang and L. Ma, *International Journal of Hydrogen Energy*, 2012, **37**, 5050-5055, DOI: 10.1016/j.ijhydene.2011.12.010.
- 27 L. Schlapbach and T. Riesterer, *Applied Physics A*, 1983, DOI: 10.1007/BF00820257.
- 28 M.O. De Marco, Y. Li, H-W Li, K. Edalati and R. Floriano, *Advanced Engineering Materials*, 2020, DOI: 10.1002/adem.201901079.
- 29 J. Liu, J. Xu, S. Sleiman, F. Ravalison, W. Zhu, H. Liu, H. Cheng and J. Huot, *International Journal of Hydrogen Energy*, 2022, **47**, 25471-25878, DOI: 10.1016/j.ijhydene.2022.06.013.
- 30 J. Liu, J. Xu, S. Sleiman, X. Chen, S. Zhu, H. Cheng and J. Huot, *International Journal of Hydrogen Energy*, 2021, **46**, 28709-28718, DOI: 10.1016/j.ijhydene.2021.06.137.
- 31 H. Zhao, P. Yao, Y. Zhao, Z. Zeng, C. Xia and T. Yang, *Alloys and Compounds*, 2023, DOI: 10.1016/j.jallcom.2023.170665.
- 32 H-L. Chen, H. Mao and Q. Chen, *Materials Chemistry and Physics*, 2018, **210**, 279- 286, DOI: 10.1016/j.matchemphys.2017.07.082.
- 33 G. Zepon, D.R. Leiva, R.B. Strozi, A. Bedoch, S.J.A. Figueroa, T.T. Ishikawa and W.J. Botta, *International Journal of Hydrogen Energy*, 2018, **43**, 1702-1708, DOI: 10.1016/j.ijhydene.2017.11.106.
- 34 J. Chen, H. Huang, T. Xu, Y. Lv, B. Liu, B. Zhang, J. Yuan and Y. Wu, *International Journal of Hydrogen Energy*, 2024, **50**, 1223-1233, DOI: 10.1016/j.ijhydene.2023.09.121.
- 35 A. Martinez-Garcia, I. Estrada-Guel, E. Reguera, R. Amaro-Hernandez, S. González, C.G. Garay-Reyes and R. Martínez-Sánchez, *International Journal of Hydrogen Energy*, 2024, **50**, 670-684, DOI: 10.1016/j.ijhydene.2023.07.341.
- 36 Z. Wang, Y. Huang, Y. Yang, J. Wang and C.T. Liu, *Scripta Materialia*, 2015, **94**, 28-31, DOI: 10.1016/j.scriptamat.2014.09.010.
- 37 M.G. Poletti and L. Battezzati, *Acta Materialia*, 2014, **75**, 297-306, DOI: 10.1016/j.actamat.2014.04.033.
- 38 I. Toda-Caraballo and P.E.J. Rivera-Díaz-del-Castillo, *Intermetallics*, 2016, **71**, 76-87, DOI: 10.1016/j.intermet.2015.12.011.
- 39 D.J.M. King, S.C. Middleburgh, A.G. McGregor and M.B. Cortie, *Acta Materialia*, 2016, **104**, 172-179, DOI: 10.1016/j.actamat.2015.11.040.
- 40 J. Ma and C. Huang, *Journal of Energy Storage*, 2023, **66**, 107419, DOI: 10.1016/j.est.2023.107419.

- 41 G. Zepon, B.H. Silva, C. Zlotea, W.J. Botta and Y. Champion, *Acta Materialia*, 2021, DOI: 10.1016/j.actamat.2021.117070.
- 42 J.B. Ponsoni, V. Aranda, T.S. Nascimento, R.B. Strozzi, W.J. Botta and G. Zepon, *Acta Materialia*, 2022, DOI: 10.1016/j.actamat.2022.118317.
- 43 A. Mohammadi, Y. Ikeda, P. Edalati, M. Mito, B. Grabowski, H-W. Li and K. Edalati, *Acta Materialia*, 2022, DOI: 10.1016/j.actamat.2022.118117.
- 44 K. Edalati, R. Floriano, P. Edalati, A. Mohammadi, Y. Li, G. Zepon and H-W. Li, *Scripta Materialia*, 2019, 387-390, DOI: 10.1016/j.scriptamat.2019.12.009.
- 45 G. Andrade, B.H. Silva, G. Zepon and R. Floriano, *International Journal of Hydrogen Energy*, 2024, **51**, 246-254, DOI: 10.1016/j.ijhydene.2023.11.111.
- 46 G. Andrade, G. Zepon, K. Edalati, A. Mohammadi, Z. Ma, H-W. Li and R. Floriano, *International Journal of Hydrogen Energy*, 2023, DOI: 10.1016/j.ijhydene.2022.12.134.
- 47 R. Floriano, G. Zepon, K. Edalati, G.L.B. Fontana, A. Mohammadi, Z. Ma, H-W. Li and R.J. Contieri, *International journal of Hydrogen Energy*, 2021, DOI: 10.1016/j.ijhydene.2021.04.181.
- 48 R. Floriano, G. Zepon, K. Edalati, G.L.B. Fontana, A. Mohammadi, Z. Ma, H-W. Li and R.J. Contieri. *International journal of hydrogen energy*, 2020, DOI: 10.1016/j.ijhydene.2020.09.047.
- 49 L. Luo, L. Chen, L. Li, S. Liu, Y. Li, C. Li, L. Li, J. Cui and Y. Li, *International Journal of Hydrogen Energy*, 2024, **50**, 406-430, DOI: 10.1016/j.ijhydene.2023.07.146.
- 50 B.H. Toby, *Powder Diffraction*, 2006, **21**, 67-70, DOI: 10.1154/1.2179804.
- 51 Y. Zhu, X-S. Yang, Z-L. Xu, G. C-P. Tsui, Q. Zhou, R. Tang, F. Xiao and K. Chan, *Journal of Energy Storage*, 2024, **75**, 109553, DOI: 10.1016/j.est.2023.109553.
- 52 J. Liang, G. Li, X. Ding, Y. Li, Z. Wen, T. Zhang and Y. Qu, *Journal of Energy Storage*, 2023, **73**, 108852, DOI: 10.1016/j.est.2023.108852.
- 53 H. Zhao, P. Yao, Y. Zhao, Z. Zeng, C. Xia and T. Yang, *Journal of Alloys and Compounds*, 2023, **960**, 170665, DOI: 10.1016/j.jallcom.2023.170665.
- 54 M. Komeili, H. Arabi and F. Pourarian, *Journal of Alloys and Compounds*, 2023, **967**, 171672, DOI: 10.1016/j.jallcom.2023.171672.
- 55 J. Garcés, *Applied Physics Letters*, 2010, 67–70, DOI:10.1063/1.3400221.
- 56 E. Akiba, *Energy Carriers and Conversion Systems*, vol. II.
- 57 S. Dangwal and K. Edalati, *Scripta Materialia*, 2024, **238**, 115774, DOI: 10.1016/j.scriptamat.2023.115774.
- 58 S. Dangwal and K. Edalati, *International Journal of Hydrogen Energy*, 2024, **50**, 626-636, DOI: 10.1016/j.ijhydene.2023.07.327.
- 59 V. Aranda, D.R. Leiva, J. Huot, W.J. Botta and G. Zepon, *Intermetallics*, 2023, **162**, 108020, DOI: 10.1016/j.intermet.2023.108020.
- 60 Y. He, Y. Su, H. Yu and C. Chen, *International Journal of Hydrogen Energy*, 2021, **46**, 7589-7600, DOI: 10.1016/j.ijhydene.2020.11.238.

61 Z.X.Ma, X.L.Xiong, L.N.Zhang, Z.H.Zhang, Y.Yan and Y.J.Su, *Electrochemistry Communications*, 2018, **92**, 24-28, DOI: 10.1016/j.elecom.2018.05.012.